

X-RAY SCALING RELATIONS OF EARLY-TYPE GALAXIES

IU. V. BABYK^{1,2,*}, B. R. MCNAMARA^{1,3}, P. E. J. NULSEN^{4,5}, M. T. HOGAN^{1,3}, A. N. VANTYGHEM¹, H. R. RUSSELL⁶, F. A. PULIDO¹,
AND A. C. EDGE⁷

¹ Department of Physics and Astronomy, University of Waterloo, 200 University Ave W, Waterloo, ON N2L 3G1, Canada

² Main Astronomical Observatory of NAS of Ukraine, 27 Academica Zabolotnogo St, 03143, Kyiv, Ukraine

³ Perimeter Institute for Theoretical Physics, 31 Caroline St N, Waterloo, ON, N2L 2Y5, Canada

⁴ Harvard-Smithsonian Center for Astrophysics, 60 Garden Str, Cambridge, MA 02138, USA

⁵ ICRAR, University of Western Australia, 35 Stirling Hwy, Crawley, WA 6009, Australia

⁶ Institute of Astronomy, Madingley Road, Cambridge, CB3 0HA, UK

⁷ Department of Physics, University of Durham, South Road, Durham DH1 3LE, United Kingdom

Draft version March 2, 2018

ABSTRACT

X-ray luminosity, temperature, gas mass, total mass, and their scaling relations are derived for 94 early-type galaxies using archival *Chandra* X-ray Observatory observations. Consistent with earlier studies, the scaling relations, $L_X \propto T^{4.5 \pm 0.2}$, $M \propto T^{2.4 \pm 0.2}$, and $L_X \propto M^{2.8 \pm 0.3}$, are significantly steeper than expected from self-similarity. This steepening indicates that their atmospheres are heated above the level expected from gravitational infall alone. Energetic feedback from nuclear black holes and supernova explosions are likely heating agents. The tight $L_X - T$ correlation for low-luminosities systems (i.e., below 10^{40} erg/s) are at variance with hydrodynamical simulations which generally predict higher temperatures for low luminosity galaxies. We also investigate the relationship between total mass and pressure, $Y_X = M_g \times T$, finding $M \propto Y_X^{0.45 \pm 0.04}$. We explore the gas mass to total mass fraction in early-type galaxies and find a range of 0.1 – 1.0%. We find no correlation between the gas-to-total mass fraction with temperature or total mass. Higher stellar velocity dispersions and higher metallicities are found in hotter, brighter, and more massive atmospheres. X-ray core radii derived from β -model fitting are used to characterize the degree of core and cuspsiness of hot atmospheres.

Keywords: galaxies: elliptical and lenticular, X-rays: galaxies

1. INTRODUCTION

In the Λ CDM cosmogony, small dark matter density fluctuations grew through the influence of gravity to create today's massive dark matter haloes. Assuming structure developed primarily by gravitational forces and that cooling was negligible, the gas temperature, luminosity, and halo mass should scale as self-similar power laws (Kaiser 1986). Atmospheric temperatures in the bremsstrahlung regime ($kT \gtrsim 2$ keV) should scale with mass as $T \propto M^{2/3}$. Likewise, X-ray luminosity should scale with temperature as $L_X \propto T^2$. Numerical simulations of hot atmospheres that respond to gravity alone have confirmed the self-similarity of the X-ray scaling relations (Evrard et al. 1996; Bryan & Norman 1998; Thomas et al. 2001; Voit et al. 2002; Voit 2005). However, observation has revealed significant deviations from self-similarity. The clearest departures are the slopes which steepen toward lower masses.

Galaxy clusters scale as $L_X \propto T^{2.7-3.0}$ and $T \propto M^{1.5-1.7}$ (Vikhlinin et al. 2006, 2009). Groups and early-type galaxies (ETGs) depart more significantly from self-similarity, $L_X \propto T^{3-5}$ and $T \propto M^{2-3}$ (Borson et al. 2011; Kim & Fabbiano 2013, and references therein). These departures indicate that processes beyond gravity alone, such as radiative cooling, supernova heating, and feedback by active galactic nuclei (AGN) are significant. Their relative contributions are unclear. However, these processes affect low mass systems the most due to the lower gravitational binding energy of their atmospheres (Giodini et al. 2013).

Numerical simulations that incorporate radio-AGN feedback are able to reproduce the observed X-ray scaling relations of clusters and ETGs quite well (Borgani et al. 2005, 2006; Sijacki & Springel 2006; Puchwein et al. 2008; Borgani & Viel 2009; Booth & Schaye 2010; Schaye et al. 2010), at least on large scales. Our understanding of radio-AGN feedback has advanced rapidly over the past decade (see e.g. McNamara & Nulsen 2007, 2012) primarily through X-ray spectral-imaging studies of hot atmospheres (Birzan et al. 2004; Rafferty et al. 2006; Shin et al. 2016; Hlavacek-Larrondo et al. 2015). X-ray cavities inflated by radio jets embedded in hot atmospheres provide an accurate measure of feedback energetics. Combined with studies of sound waves and weak shock fronts (Nulsen et al. 2005; Borgani et al. 2005, 2006; Borgani & Viel 2009; Randall et al. 2015; Fabian et al. 2017; Forman et al. 2017), this work has shown that radio AGN release enough energy to offset radiative cooling while affecting the X-ray scaling relations in clusters (Main et al. 2017).

Studies of the scaling relations have often targeted galaxy clusters and groups (O'Sullivan et al. 2001; David et al. 2006; Borson et al. 2011; Babyk & Vavilova 2014; Vavilova et al. 2015; Su et al. 2015; Goulding et al. 2016). Less massive ETGs are more difficult to study and thus have not received the same level of attention. Nevertheless, the X-ray scaling relations of ETG are sensitive to the origin and evolution of the interstellar medium of ETGs and their host galaxies (see e.g. Bender et al. 1989; Fabbiano 1989; Mathews 1990; White & Sarazin 1991; David et al. 1991; Mathews & Brighenti 2003; Khosroshahi et al. 2004, for more details). However, the X-

* ibabyk@uwaterloo.ca, babikyura@gmail.com

ray analysis of ETGs is complicated by X-ray emission from low-mass X-ray binaries (LMXBs) and other stellar sources that contribute to the total X-ray emission. Their contributions must be estimated reliably to obtain meaningful measurements of the atmospheric properties (Revnivtsev et al. 2007a, 2008a; Boroson et al. 2011; Kim & Fabbiano 2013, 2015). The immediate aim of this paper is to do just this in a longer-term effort to evaluate the degree to which AGN feedback and supernova explosions affect galaxy evolution over several decades in halo mass.

Recent studies of ETG scaling relations have concerned small samples exploring $L_X - T$, $L_X - M$, and $L_X - L_B$. Here, we perform uniform analysis 94 ETGs within $5r_e$ ² taken from the *Chandra* archive. We investigate these scaling relations in addition to $M - M_g$ and $L_X - \sigma_c$, and the first time for ETGs, $M - M_g \times T$. We further study the structural and dynamical properties of ETGs.

The paper is organized as follows. The review of our sample and data analysis is presented in Section 2. Section 3 describes the spectral analysis. The surface brightness, density, and mass calculations are described in Section 4. Section 5 describes the results of the luminosity-temperature, mass-temperature, luminosity-mass, and mass- Y_X scaling relations. The results are discussed in Section 6 and our conclusions are presented in Section 7.

We assume a standard Λ CDM cosmology with the following parameters: $H_0 = 70 \text{ km s}^{-1} \text{ Mpc}^{-1}$, $\Omega_\Lambda = 0.7$, $\Omega_M = 0.3$. The quoted measurement uncertainties refer to the 1σ confidence level, unless otherwise specified.

2. EARLY-TYPE GALAXY SAMPLE AND DATA ANALYSIS

Based on the samples of Beuing et al. (1999) and O’Sullivan et al. (2003), Nulsen et al. (2009) selected a sample of 104 nearby objects with following criteria: (1) $L_K > 10^{10} L_\odot$, (2) absolute magnitude $M_B < -19$, morphological T-type < -2 , (3) Virgo-centric flow corrected recession velocity. Only 87 objects have been observed with *Chandra*. To increase our sample we added galaxies from the ATLAS^{3D} (Cappellari et al. 2011) and MASSIVE (see Ma et al. (2014) for sample selection details) samples that were observed by *Chandra*, namely 61 and 39 targets, respectively. In total we analyzed about 150 targets. We selected observations with cleaned exposure times above 10 ks in order to eliminate large uncertainties during spectral analysis. This excludes about half of the targets from the ATLAS^{3D} sample. Our final sample contains 94 objects, which is 1.5 times larger than previous studies of X-ray scaling relations in ETGs. We used LEDA³, SIMBAD⁴ and NED⁵ databases to classify the objects. The observations have been downloaded from the HEASARC⁶ archive.

The final ETG sample is shown in Table 1. The angular and luminosity distances are measured using redshifts from NED. We assumed $D_A = 16.5$ and $D_L = 17.5$ Mpc for Virgo galaxies (see Cappellari et al. 2011; marked with star in columns 10 and 11). We include several non-Virgo galaxies whose redshifts are too low to respond reliably to the Hubble flow: NGC1386, NGC3079, NGC4278, NGC4457, and NGC4710. For these we use distances derived from surface brightness

fluctuations (Mei et al. 2007). Our sample covers a wide range of distance and includes elliptical, lenticular, SB, BCGs, and cD galaxies. In some cases the morphological type differs between NED and SIMBAD. For example, NGC383, NGC507, NGC3665, NGC4382, NGC4477, and NGC4526 are classified by NED as SAB0 galaxies, while in SIMBAD these objects were classified as S0. We have found about 30 galaxies with discrepant morphological classifications. Kim & Fabbiano (2015) claimed that these disparities indicate misclassification due to dust obscuration and/or hidden disks.

The galactic coordinates taken from SIMBAD were derived using data from the 2MASS⁷ survey. These coordinates are consistent with the optically-derived coordinates from NED. However, in some objects the location of the peak X-ray emission differs from the optically coordinates. This difference is generally insignificant, so has been neglected.

2.1. Optical data processing

Effective radii, r_e , were measured using optical Digitized Sky Survey (*DSS*) images. $10' \times 10'$ images were downloaded from the *ESO* web-page⁸. No additional calibrations were performed on these images. Surface brightness profiles centered on the peak of the optical emission were extracted from each image. The background emission was obtained by fitting a constant to the outskirts of each profile and subtracted from each image. The total flux was determined by numerically integrating the profile including light significantly above background by 5σ . Uncertainties on r_e were determined using 1000 Monte Carlo realizations of the surface brightness profiles. The $5r_e$ measurements and their uncertainties are presented in second column of Table 2.

2.2. X-ray data processing

Chandra observations were analyzed using the CIAO software package version 4.8 and CALDB version 4.7.1. *Chandra* data from the Advanced CCD Imaging Spectrometer (ACIS) were analyzed, apart from early observations with CCD temperatures above -120°C . All galaxies were observed using ACIS chips 3 and 7. Level-2 event files were produced by correcting the level-1 event files for time-dependent gain and charge transfer inefficiency. Level-2 event files were filtered to delete bad grades. VFaint filtering was performed as necessary. Background flares were identified and removed using the LC_CLEAN⁹ tool provided by M. Markevitch. Blank-sky background files were extracted for each observation and processed identically to the target files. Background files were reprojected to the corresponding position, and then normalized to match the 9.5-12.0 keV flux. Column 5 of Table 1 shows the exposure time before and after corrections were applied.

X-ray images of the ETGs were formed by summing all events within the 0.5 – 6.0 keV energy range. Point sources were removed using the *wavdetect* routine with a significance threshold of 10^{-6} . Spectra were extracted from circular regions encompassing the central $5r_e$ of each galaxy. Background spectra were obtained from a nearby region free of sources with the same area as the source region. The local backgrounds are consistent with the blank-sky backgrounds used for creating images. The source and background spectra, the ancillary reference files (*ARF*), and redistribution matrix

² Here, r_e is the half-light radius.

³ Lyon-Meudon Extragalactic Database, Paturel et al. (1997)

⁴ <http://simbad.u-strasbg.fr/>

⁵ <https://ned.ipac.caltech.edu/>

⁶ <http://heasarc.gsfc.nasa.gov/>

⁷ The Two Micron All Sky Survey at near-infrared wavelengths

⁸ <http://archive.eso.org/dss/dss>

⁹ <http://cxc.cfa.harvard.edu/contrib/maxim/acisbg/>

Table 1
List of early-type galaxy properties.

Name	RA (J2000)	DEC (J2000)	ObsID	Exposure ks before/after	Type	BCG	cD	z	D_A Mpc	D_L Mpc	N_H 10^{20} cm^{-2}
(1)	(2)	(3)	(4)	(5)	(6)	(7)	(8)	(9)	(10)	(11)	(12)
ESO3060170	246.41	-30.289	multi	28.05/25.96	E3	✓		0.035805	145.1	155.7	3.51/13.4
IC1262	69.5188	32.0738	multi	113.68/106.17	E	✓		0.032649	133.0	141.8	2.47/21.2
IC1459	4.6590	-64.1096	2196	58.83/45.14	E3			0.006011	25.503	25.8	1.19/1.68
IC1633	293.098	-70.8424	4971	24.79/22.24	E1	✓	✓	0.02425	100.0	104.9	2.01/5.34
IC4296	313.5384	27.9729	multi	48.53/40.05	E			0.012465	52.358	53.7	4.11/12.4
IC5267	350.2369	-61.801	3947	54.97/43.71	SA0			0.005711	24.241	24.5	1.62/1.91
IC5358	25.1415	-75.8683	multi	39.61/38.82	E4	✓	✓	0.02884	118.1	125.0	1.54/7.2
NGC315	124.5631	-32.4991	4156	55.02/39.49	E		✓	0.016485	68.816	71.1	5.87/48.2
NGC326	124.8444	-35.9797	6830	90.83/90.83	E	✓	✓	0.047400	188.8	207.1	5.81/68.7
NGC383	126.8391	-30.3379	2147	44.41/41.29	S0			0.017005	70.930	73.4	5.42/21.5
NGC499	130.4977	-28.9448	multi	38.62/38.48	E5			0.014673	61.423	63.2	5.26/13.6
NGC507	130.6430	-29.1326	317	43.63/40.30	S0	✓		0.016458	68.706	71.0	5.32/13.7
NGC533	140.1457	-59.9683	2880	37.61/28.40	E3		✓	0.018509	77.025	79.9	3.12/24.7
NGC708	136.5695	-25.0903	multi	139.43/137.38	E	✓	✓	0.016195	67.635	69.8	5.37/11.5
NGC720	173.0194	-70.3572	multi	99.21/98.22	E5			0.005821	24.704	25.0	1.55/13.9
NGC741	150.9342	-53.6764	2223	30.35/28.14	E0			0.018549	77.186	80.1	4.47/59.2
NGC821	151.5555	-47.5568	multi	188.31/181.64	E6			0.005787	24.561	24.8	6.34/13.0
NGC1023	145.0232	-19.0892	multi	616.18/188.09	SB0			0.002125	16.5*	17.5*	7.17/4.26
NGC1265	150.1336	-13.1299	3237	93.86/93.60	E		✓	0.025137	103.6	108.8	14.3/5.25
NGC1266	183.6680	-47.5077	11578	153.60/28.63	SB			0.007238	30.649	31.1	5.39/7.16
NGC1316	240.1627	-56.6898	2022	29.86/21.21	S0			0.005871	24.914	25.2	1.92/48.4
NGC1332	212.1830	-54.3661	multi	74.82/20.48	S0			0.005084	21.601	21.8	2.29/26.8
NGC1386	237.6634	-53.9659	multi	80.81/70.47	SB			0.002895	16.5*	17.5*	1.39/181.0
NGC1399	236.7164	-53.6356	9530	59.35/56.98	E1	✓		0.004753	20.205	20.4	1.31/163.0
NGC1404	236.9552	-53.5548	multi	319.27/296.7	E1			0.006494	27.531	27.9	1.35/163.0
NGC1407	209.6362	-50.3838	14033	54.35/50.26	E0			0.005934	25.179	25.5	5.41/17.3
NGC1482	214.1238	-47.8035	2932	28.20/15.36	SA0			0.006391	27.099	27.4	3.73/10.3
NGC1550	190.9760	-31.8488	multi	89.00/89.00	SA0	✓		0.012389	52.045	53.3	11.2/5.98
NGC1600	200.4164	-33.2418	4371	26.75/24.57	E3			0.015614	65.267	67.3	4.71/4.85
NGC1700	203.6991	-27.6137	2069	42.81/26.79	E4			0.012972	54.445	55.9	4.80/5.06
NGC2434	281.0002	-21.5444	2923	52.44/47.31	E0			0.004637	19.716	19.9	12.1/15.5
NGC2768	155.4947	40.5634	9258	153.92/63.56	E6			0.004513	19.191	19.4	3.89/0.97
NGC3079	157.8101	48.3598	2038	33.02/23.51	SB			0.003723	16.5*	17.5*	0.80/1.36
NGC3091	256.7559	27.5029	3215	31.69/27.34	E3	✓		0.013222	55.473	56.9	4.75/4.79
NGC3379	233.4901	57.6328	multi	369.63/319.34	E1			0.003039	16.5*	17.5*	2.75/1.59
NGC3384	233.5221	57.7524	multi	121.55/115.82	SB0			0.002348	16.5*	17.5*	2.75/1.75
NGC3557	281.5784	21.0890	4502	99.41/93.86	E3			0.010300	43.410	44.3	7.44/16.7
NGC3585	277.2465	31.1753	9506	61.23/57.96	E6			0.004783	20.332	20.5	5.57/8.49
NGC3607	230.5996	66.4223	2073	38.50/32.69	SA0			0.003142	22.2	23.5	1.52/2.60
NGC3665	174.7122	68.4932	3222	17.96/14.59	SA0			0.006901	29.238	29.6	2.07/1.38
NGC3923	287.2759	32.2224	9507	81.00/80.90	E4			0.005801	24.620	24.9	6.29/11.6
NGC3955	286.1398	37.8258	2955	19.71/19.29	S0			0.004973	21.133	21.3	4.86/8.40
NGC4036	132.9794	54.2466	6783	21.84/12.20	S0			0.004620	19.643	19.9	1.90/2.64
NGC4073	276.9081	62.3697	3234	29.96/25.76	E	✓	✓	0.019584	81.364	84.6	1.90/3.91
NGC4104	204.3284	80.0306	6939	35.88/34.86	S0	✓		0.028196	115.6	122.2	1.68/2.58
NGC4125	130.1897	51.3391	2071	64.23/52.97	E6			0.004523	19.234	19.4	1.86/3.13
NGC4203	173.0323	80.0788	10535	42.12/40.61	SAB0			0.003623	17.28	17.5	1.20/4.08
NGC4261	281.8049	67.3726	9569	102.55/102.24	E2			0.007378	31.236	31.7	1.56/5.50
NGC4278	193.7824	82.7727	multi	470.84/462.52	E1			0.002068	17.11	17.4	1.75/6.03
NGC4325	279.5840	72.1969	3232	30.09/28.30	E	✓		0.025714	105.8	111.3	2.18/5.39
NGC4342	283.4824	68.8699	12955	54.54/53.35	S0			0.002538	16.5	17.5	1.61/5.31
NGC4365	283.8070	69.1819	2015	40.43/37.36	E3			0.004146	17.642	17.8	1.61/5.44
NGC4374	278.2045	74.4784	multi	87.02/79.85	E1			0.003392	16.5*	17.5*	2.58/6.02
NGC4382	267.7120	79.2372	2016	39.75/29.33	SA0			0.002432	16.5*	17.5*	2.51/3.99
NGC4388	279.1220	74.3355	9276	170.59/170.59	SAB			0.008419	35.586	36.2	2.58/6.52
NGC4406	279.0835	74.6369	318	15.02/13.13	E3			0.000747	16.5*	17.5*	2.58/6.36
NGC4457	289.1324	65.8389	3150	38.88/32.50	SAB			0.002942	16.5*	17.5*	1.84/5.53

Table 1
Continued.

Name	RA (J2000)	DEC (J2000)	ObsID	Exposure ks before/after	Type	BCG	cD	z	D_A Mpc	D_L Mpc	N_H 10^{20} cm 2
(1)	(2)	(3)	(4)	(5)	(6)	(7)	(8)	(9)	(10)	(11)	(12)
NGC4472	286.9222	70.1961	11274	39.67/39.67	E2			0.003272	16.5*	17.5*	1.65/7.71
NGC4477	281.5441	75.6119	9527	38.10/37.68	SB0			0.004463	18.980	19.2	2.63/6.38
NGC4486	283.7777	74.4912	2707	90.03/89.09	E0		✓	0.004283	18.220	18.4	2.52/7.36
NGC4526	290.1595	70.1385	3925	43.53/31.73	SAB			0.002058	16.5*	17.5*	1.66/7.78
NGC4552	287.9326	74.9668	multi	146.96/145.93	E0			0.001134	16.5*	17.5*	2.56/6.34
NGC4555	221.8117	86.4343	2884	29.97/23.91	E			0.022292	92.231	96.4	1.37/5.95
NGC4564	289.5604	73.9207	4008	16.02/15.84	E6			0.003809	15.8	16.3	2.27/6.85
NGC4621	294.3646	74.3621	2068	24.84/24.84	E5			0.001558	16.5*	17.5*	2.22/6.90
NGC4636	297.7485	65.4729	multi	149.07/133.43	E0			0.003129	14.5	15.2	1.83/8.12
NGC4649	295.8736	74.3178	multi	69.88/61.60	E2			0.003703	16.5*	17.5*	2.13/7.19
NGC4696	302.4036	21.5580	1560	84.75/21.20	E1	✓	✓	0.009867	41.613	42.4	8.07/23.5
NGC4697	301.6329	57.0637	4730	40.05/36.98	E6			0.00414	17.616	17.8	2.12/15.7
NGC4710	300.8506	78.0300	9512	29.47/27.72	SA0			0.003676	16.5	17.5	2.15/8.24
NGC4782	304.1379	50.2958	3220	49.33/49.33	E0			0.015437	64.545	66.6	3.56/31.8
NGC4936	306.2037	32.2638	multi	28.92/25.14	E0			0.010397	43.812	44.7	5.91/49.9
NGC5018	309.8982	43.0614	2070	30.89/26.54	E3			0.009393	39.643	40.4	6.98/114.0
NGC5044	311.2340	46.0996	multi	316.04/302.07	E0	✓		0.00928	39.173	39.9	5.03/112.0
NGC5171	334.8063	72.2182	3216	34.67/30.58	S0			0.022943	94.830	99.2	1.92/30.8
NGC5353	82.6107	71.6336	14903	40.27/37.20	S0			0.007755	32.813	33.3	0.98/8.39
NGC5532	357.9614	64.1119	3968	49.36/44.53	S0			0.024704	101.8	106.9	1.86/68.2
NGC5813	359.1820	49.8484	multi	488.04/481.82	E1			0.006525	27.662	28.0	4.23/10.9
NGC5846	0.3389	48.9043	7923	90.01/85.25	E	✓		0.00491	20.867	21.1	4.24/8.73
NGC5866	92.0340	52.4891	2879	27.43/25.55	S0			0.002518	14.9	15.2	1.45/15.4
NGC6098	34.9745	42.8152	10230	44.57/43.12	E		✓	0.030851	126.0	133.9	4.18/7.56
NGC6107	56.2296	45.6870	8180	20.87/19.29	E	✓	✓	0.030658	125.2	133.0	1.46/37.8
NGC6251	115.7638	31.1958	4130	45.44/14.06	E			0.024710	101.9	107.0	5.40/4.31
NGC6269	49.0135	35.9380	4972	39.64/35.80	E		✓	0.034801	141.3	151.3	4.65/12.8
NGC6278	43.5694	33.945	6789	15.04/11.79	S0			0.009447	39.865	40.6	4.91/7.29
NGC6338	85.8062	35.3991	4194	47.33/44.52	S0			0.027303	112.1	118.3	2.55/45.4
NGC6482	48.0905	22.9122	3218	19.34/10.03	E			0.013129	55.091	56.5	8.04/9.85
NGC6861	350.8772	-32.2109	11752	93.50/88.89	SA0			0.009437	39.826	40.6	4.94/1.22
NGC6868	350.9126	-32.6376	11753	72.60/69.53	E2	✓		0.009520	40.171	40.9	4.94/1.27
NGC7176	14.9320	-53.0969	905	49.53/43.63	E			0.008376	35.406	36.0	1.61/2.42
NGC7196	345.3695	-51.0861	10546	10.11/10.11	E			0.009750	41.127	41.9	1.84/0.87
NGC7618	105.5754	-16.9091	multi	235.84/168.14	E			0.017309	72.164	74.7	11.9/38.1
NGC7626	87.8591	-48.3788	2074	26.74/23.61	E			0.011358	47.790	48.9	4.94/5.37
UGC408	116.977	-59.40	11389	93.92/93.80	SAB0			0.014723	61.628	63.5	2.80/13.6

files (*RMF*), were created using the *specextract* task in the CIAO package. Spectra were grouped with one count per energy bin.

3. SPECTRAL ANALYSIS

3.1. Multi-component spectral modeling

Previous studies of the X-ray emission from low-mass systems showed that the unresolved LMXBs and other stellar sources including active binaries (ABs) and cataclysmic variables (CVs) contribute to the total X-ray emission (Pellegrini & Fabbiano 1994; Revnivtsev et al. 2008a). Due to their low X-ray luminosities, $\sim 10^{37-38}$ erg/s, LMXBs, ABs, and CVs were often ignored. However, our sample includes gas-poor galaxies ($L_X < 10^{40}$ erg/s), so we must account for stellar sources. Their fluxes have been measured directly in M31, M32, and the Galactic bulge (Revnivtsev et al. 2007a; Boroson et al. 2011). All LMXBs in these galaxies were detected using a combination of thermal and non-thermal (power law) models. Revnivtsev et al. (2008a) measured the temperature of the unresolved stellar sources to be $kT = 0.48 \pm 0.07$ keV. The power law slope of the non-thermal component is $\Gamma = 1.76 \pm 0.37$. These studies showed that power law and thermal models provide good fits to the X-ray emission of both resolved and unresolved LMXBs. Later, Wong et al. (2014) found that a Γ_{LMXBs} in the range 1.4 – 1.8 provided similar results for the hot atmosphere. We applied these and other previous measurements in our spectral fitting.

We use a multi-component model of the form PHABS*(APEC+PO+MEKAL+PO) to fit an each spectrum of sampled targets in the XSPEC version 12.9.1 environment (Arnaud 1996). Here APEC models the thermal emission from the atmosphere, the first PO is a power law that describes emission from LMXBs, and MEKAL+PO describes the thermal (MEKAL) and non-thermal (PO) contribution from ABs and CVs. The PHABS model accounts for photoelectric absorption and was fixed to the hydrogen column densities shown in the last column of Table 1 as first value. They were obtained from Dickey & Lockman (1990). The temperature and metallicity of the APEC model were free parameters. The slopes of two PO models were fixed to 1.6 and 1.9, respectively. When metallicity was poorly constrained by the model, it was fixed to $0.5Z_{\odot}$. This value was chosen following Boroson et al. (2011) and Werner et al. (2012). The temperature and metallicity in the MEKAL model were fixed to 0.5 keV and $0.3Z_{\odot}$, respectively. All frozen parameters used in this spectral fitting were previously tested and applied in previous analyses (e.g. Revnivtsev et al. 2008a; Boroson et al. 2011; Kim & Fabbiano 2013; Wong et al. 2014). The Cash-statistic¹⁰ (Cash 1979) was applied in spectral fitting.

The spectra were well-fit by this model ($\chi^2 \approx 1$, χ^2 in *C*-statistic is *C*-stat value divided by degrees of freedom) apart from ten objects: NGC708, NGC1399, NGC3557, NGC4388, NGC4472, NGC4636, NGC4649, NGC5044, NGC5813, and NGC6251. These are among the brightest in the sample. Regrouping the spectra to 50 counts per energy bin, compared to the previous 1 per bin, reduces the χ^2 to about 1 while maintaining the same temperature and flux measurements.

The temperature of ETGs here ranges between 0.20 keV in NGC821 and NGC1023 to 3.34 keV in IC5358. ESO3060170, IC5358, NGC6269, and NGC6278 have been excluded because their temperatures exceed >2 keV, presum-

ably because of a larger scale hot atmosphere (Werner et al. 2012). Unabsorbed X-ray fluxes, f_X , in the 0.5 – 2.0 keV energy band were measured by adding a CFLUX component to the original model. This energy band was chosen for consistency with previous papers. We extracted the X-ray fluxes in the 0.5 – 6 keV range, and found only a 1% to 2% discrepancy with the 0.5 – 2.0 keV flux. In both cases the spectra were fit over the entire 0.5 – 6.0 keV energy range. The corresponding X-ray luminosity was then determined from $L_X = 4\pi D_L^2 f_X$. Our sample spans a wide range of X-ray luminosities, $(0.02 - 391) \times 10^{40}$ erg/s. The best-fitting parameters from this spectral analysis are shown in Table 2.

The spectral analysis was also performed using MEKAL instead of APEC to model the thermal emission from the hot cluster gas. This approach permits a comparison to previous measurements, and to test systematic differences between the two thermal models. We found that APEC temperatures are 10-20% higher than those measured using MEKAL. In contrast, the X-ray flux provided by both these models are equal within uncertainties. The temperature differences are likely due to out-of-date atomic libraries in the MEKAL model. We have used APEC version 3.0.7, which contains the most up-to-date atomic libraries, as well as photoionization and recombination rates.

An APEC model was used to fit the thermal emission from stellar sources to check the MEKAL results. The previous temperature and flux measurements of the hot gas were than compared with the new spectral model (i.e., PHABS*(APEC+PO+APEC+PO)). We found that using APEC to model the thermal component of stellar sources, with all other parameters fixed to their previous values, provides essentially the same temperatures and fluxes for the thermal component of the hot gas. Thus, we adopt our primary model for consistency with previous results.

3.2. Comparison with previous results

Of our sample of 94, 56 objects have previous temperature and luminosity measurements. These values are taken from Fukazawa et al. (2006); Boroson et al. (2011); Su & Irwin (2013); Kim & Fabbiano (2015); Goulding et al. (2016), referred to as F06, BKF11, SI13, KF15, G16, respectively, in Fig. 1. Our measurements generally agree well with earlier studies. However, our the temperatures are slightly higher than previous results. This small discrepancy might be due to several factors including: (1) use of the *C*-statistic instead of χ^2 in our spectral analysis; (2) adopting different fixed parameters in our multi-component model; (3) using the MEKAL model instead APEC; or (4) using different energy ranges during spectral fitting.

To investigate the impact of fixing the foreground extinction, N_H , to the Dickey & Lockman (1990) values, we performed additional spectral fitting allowing N_H to vary. The best-fitting N_H values are systematically 1.5-2 times higher than those obtained by Dickey & Lockman (1990). Nevertheless, the choice of fixing N_H or allowing it to vary affected the slope, zero point, and scatter on the derived temperatures and luminosities insignificantly. The fixed and free values for the zero point are 0.08 ± 0.03 , 0.06 ± 0.03 , slope, 1.23 ± 0.13 , 1.28 ± 0.14 , and scatter, 0.44 ± 0.04 and 0.42 ± 0.04 , respectively.

The Dickey & Lockman (1990) values of N_H have been surpassed by the Leiden/Argentine/Bonn radio survey by Kalberla et al. (2005). In addition, molecular hydrogen and

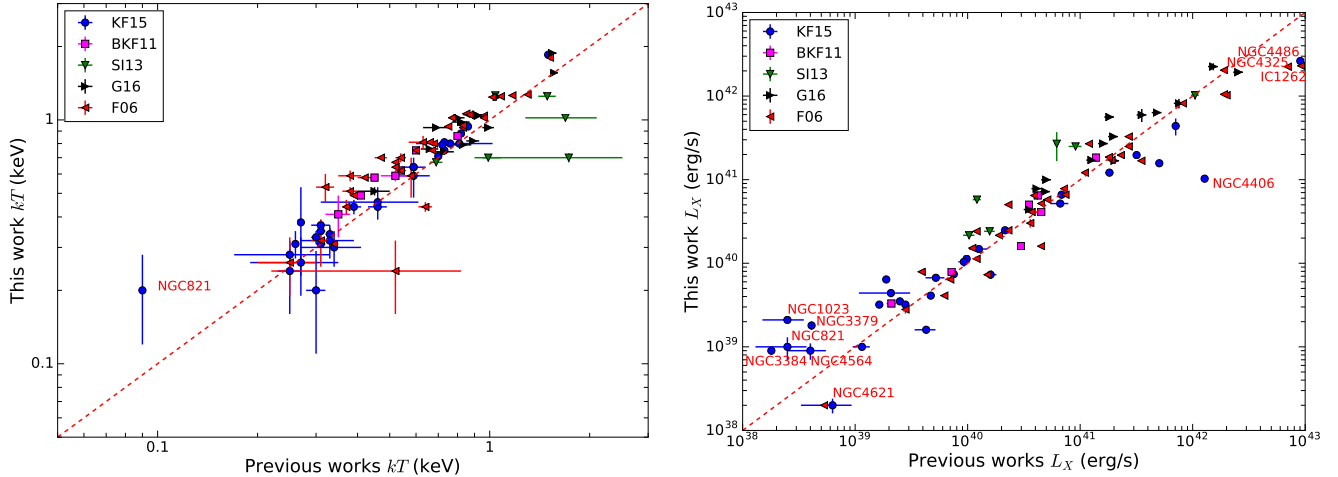
¹⁰ <http://cxc.harvard.edu/sherpa/ahelp/cstat.html>

Table 2
The best-fit parameters for spectra extracted from within $5r_e$. The central velocity dispersion, σ , was taken from LEDA.

Name	$5r_e$ kpc	T_X keV	f_X 0.5-2.0 keV erg/cm ² /s	L_X 10 ⁴⁰ erg/s	Z Z_\odot	χ^2 $C-stat/d.o.f.$	σ km/s
(1)	(2)	(3)	(4)	(5)	(6)	(7)	(8)
ESO3060170	89±7	2.40±0.11	-11.88±0.01	382.37±8.80	0.69±0.13	1.2	271.7±13.2
IC1262	123±13	1.80±0.05	-12.02±0.006	229.75±3.17	0.45±0.05	1.2	232.5±9.6
IC1459	35±6	0.70±0.01	-12.52±0.01	2.41±0.06	0.07±0.01	1.1	293.6±6.3
IC1633	135±25	1.84±0.14	-12.40±0.02	52.42±2.41	0.72±0.21	1.0	356.6±12.4
IC4296	77±9	0.94±0.01	-12.28±0.01	18.11±0.42	0.29±0.05	1.1	327.1±5.4
IC5267	38±6	0.48±0.12	-13.27±0.03	0.39±0.03	0.11±0.07	1.0	167.7±5.2
IC5358	250±32	3.34±0.06	-11.43±0.003	694.59±4.80	0.66±0.06	1.3	214.2±5.0
NGC315	88±19	0.76±0.01	-12.35±0.007	27.02±0.44	0.19±0.02	1.5	293.3±0.2
NGC326	191±33	0.94±0.10	-13.80±0.07	8.13±1.31	0.5	1.0	231.9±13.1
NGC383	48±5	0.98±0.02	-12.81±0.01	9.98±0.23	0.5	1.0	271.9±6.7
NGC499	57±8	0.79±0.01	-11.93±0.007	56.15±0.91	0.48±0.07	1.9	253.3±6.7
NGC507	107±12	1.25±0.01	-11.77±0.004	102.43±0.94	0.56±0.04	1.2	291.8±5.9
NGC533	112±15	1.04±0.004	-11.97±0.004	81.85±0.75	0.41±0.03	1.4	271.2±5.6
NGC708	110±14	1.56±0.01	-11.48±0.002	193.03±0.89	0.65±0.02	3.1	222.2±7.8
NGC720	32±3	0.62±0.01	-12.26±0.006	4.11±0.06	0.26±0.03	1.1	235.6±5.6
NGC741	88±7	1.02±0.01	-12.37±0.008	32.75±0.60	0.25±0.03	1.1	286.0±9.3
NGC821	30±7	0.20±0.08	-13.85±0.12	0.10±0.03	0.5	0.9	198.4±2.8
NGC1023	35±4	0.20±0.09	-13.25±0.03	0.21±0.02	0.5	1.1	197.9±4.6
NGC1265	143±17	0.96±0.04	-13.28±0.03	7.43±0.51	0.5	1.1	-
NGC1266	13±2	0.80±0.03	-13.23±0.03	0.67±0.05	0.5	0.9	94.4±5.2
NGC1316	58±7	0.75±0.01	-12.07±0.006	6.47±0.09	0.22±0.02	1.2	223.7±3.3
NGC1332	30±4	0.70±0.03	-12.42±0.007	2.16±0.04	0.15±0.02	1.1	312.5±10.7
NGC1386	16±4	0.32±0.04	-13.20±0.04	0.23±0.02	0.5	1.1	166.2±18.0
NGC1399	45±5	1.26±0.003	-11.30±0.002	24.96±0.12	0.46±0.01	2.9	333.7±5.3
NGC1404	45±5	0.67±0.004	-11.54±0.003	26.86±0.19	0.19±0.007	1.6	228.1±3.6
NGC1407	44±5	1.02±0.02	-12.13±0.01	5.77±0.13	0.19±0.03	1.4	264.9±5.1
NGC1482	69±7	0.80±0.01	-12.64±0.01	2.06±0.05	0.5	1.6	108.5±7.4
NGC1550	54±5	1.27±0.005	-11.51±0.003	105.04±0.73	0.48±0.02	1.4	300.3±5.3
NGC1600	97±10	1.24±0.02	-12.49±0.01	17.14±0.40	0.32±0.05	1.1	331.4±7.0
NGC1700	45±6	0.51±0.02	-12.68±0.01	7.81±0.18	0.13±0.03	1.1	233.1±3.9
NGC2434	25±3	0.59±0.03	-12.78±0.02	0.79±0.04	0.5	1.2	183.7±5.3
NGC2768	31±4	0.35±0.02	-12.7848±0.01	0.74±0.02	0.5	1.1	184.2±2.8
NGC3079	25±4	0.78±0.01	-12.58±0.01	0.97±0.02	0.5	1.7	175.1±12.3
NGC3091	47±6	0.88±0.01	-12.14±0.006	28.06±0.39	0.57±0.08	1.0	310.2±7.6
NGC3379	29±5	0.24±0.08	-13.31±0.05	0.18±0.02	0.11±0.08	1.4	203.7±1.8
NGC3384	23±3	0.31±0.04	-13.59±0.05	0.09±0.01	0.5	1.0	145.7±2.5
NGC3557	60±7	0.43±0.10	-12.68±0.06	4.91±0.67	0.5	2.2	264.1±7.2
NGC3585	35±4	0.32±0.07	-13.25±0.04	0.28±0.03	0.5	1.1	210.9±6.2
NGC3607	28±3	0.59±0.11	-12.75±0.02	0.73±0.03	0.5	1.1	220.8±4.2
NGC3665	38±5	0.30±0.05	-12.85±0.03	1.48±0.10	0.5	0.9	214.7±8.6
NGC3923	50±6	0.58±0.01	-12.17±0.005	5.02±0.06	0.18±0.02	1.5	246.6±5.6
NGC3955	11±1	0.31±0.03	-13.41±0.04	0.21±0.02	0.5	0.9	94.4±5.3
NGC4036	18±2	0.46±0.07	-13.46±0.06	0.16±0.01	0.5	0.7	197.9±6.3
NGC4073	104±16	1.88±0.02	-11.58±0.003	225.24±1.56	1.67±0.10	1.5	267.0±6.3
NGC4104	132±14	1.43±0.04	-12.38±0.01	74.48±1.71	0.30±0.04	1.3	291.0±5.5
NGC4125	32±3	0.49±0.01	-12.45±0.007	1.60±0.03	0.18±0.02	1.0	238.2±7.0
NGC4203	21±3	0.28±0.03	-12.92±0.02	0.44±0.02	0.5	1.0	160.8±5.5
NGC4261	45±4	0.80±0.006	-12.26±0.005	6.61±0.08	0.19±0.01	1.5	296.4±4.3
NGC4278	25±3	0.33±0.02	-13.02±0.01	0.35±0.01	0.5	1.0	234.3±4.5
NGC4325	16±1	0.93±0.006	-11.82±0.004	224.34±2.07	0.51±0.04	0.9	-
NGC4342	11±1	0.64±0.02	-13.06±0.01	0.32±0.01	0.16±0.04	1.0	240.7±5.7
NGC4365	28±2	0.44±0.02	-12.97±0.02	0.41±0.02	0.5	1.1	246.9±2.6
NGC4374	32.51±3	0.81±0.005	-11.85±0.004	5.18±0.05	0.16±0.007	1.4	274.9±2.4
NGC4382	34±3	0.44±0.03	-12.51±0.01	1.13±0.03	0.23±0.05	1.1	175.3±3.5
NGC4388	39±4	0.98±0.05	-12.63±0.03	3.68±0.25	0.5	4.9	98.9±9.4
NGC4406	35±3	0.88±0.01	-11.55±0.01	10.28±0.24	0.34±0.03	1.1	230.0±2.6
NGC4457	18±2	0.59±0.02	-12.83±0.02	0.54±0.03	0.17±0.05	1.1	113.3±9.8

Table 2
Continued.

Name	$5r_e$ kpc	T_X keV	f_x 0.5-2.0 keV erg/cm ² /s	L_X 10 ⁴⁰ erg/s	Z Z_\odot	χ^2 $C-stat/d.o.f.$	σ km/s
(1)	(2)	(3)	(4)	(5)	(6)	(7)	(8)
NGC4472	36±3	1.06±0.002	-11.30±0.002	18.36±0.08	0.55±0.02	3.0	280.8±2.9
NGC4477	21±3	0.34±0.02	-12.63±0.01	1.04±0.03	0.5	1.1	172.2±6.2
NGC4486	35±4	1.85±0.002	-10.19±0.0003	262.93±0.18	0.75±0.004	4.3	321.7±4.3
NGC4526	25±3	0.37±0.02	-13.06±0.02	0.32±0.02	0.5	1.2	224.4±9.4
NGC4552	24±2	0.64±0.01	-12.17±0.007	2.48±0.04	0.16±0.02	1.2	249.7±2.9
NGC4555	63±7	1.05±0.02	-12.82±0.01	16.83±0.33	0.33±0.07	1.3	344.0±28.5
NGC4564	13±3	0.38±0.15	-13.61±0.11	0.09±0.02	0.5	0.9	155.9±2.2
NGC4621	24±3	0.26±0.07	-13.65±0.09	0.02±0.004	0.5	1.1	227.7±3.8
NGC4636	34±3	0.75±0.003	-11.27±0.002	19.68±0.09	0.42±0.02	1.7	199.7±2.7
NGC4649	41±4	0.94±0.003	-11.48±0.002	12.13±0.06	0.58±0.03	2.0	329.1±4.6
NGC4696	64±5	1.88±0.02	-10.74±0.003	391.42±2.70	0.86±0.04	2.2	243.8±6.5
NGC4697	35±3	0.31±0.01	-12.77±0.02	0.64±0.03	0.5	1.1	166.6±1.6
NGC4710	17±2	0.32±0.05	-13.56±0.06	0.10±0.01	0.5	1.1	116.5±6.4
NGC4782	64±3	1.02±0.01	-12.65±0.01	11.88±0.28	0.5	1.8	308.5±11.2
NGC4936	69±4	0.91±0.04	-12.31±0.02	11.71±0.54	0.22±0.09	0.8	278.2±14.8
NGC5018	39±4	0.53±0.07	-13.11±0.03	1.52±0.10	0.5	1.1	206.5±4.5
NGC5044	51±3	0.95±0.002	-10.97±0.002	204.11±0.47	0.35±0.007	3.5	225.7±9.2
NGC5171	88±7	0.81±0.05	-13.59±0.05	3.02±0.35	0.5	0.7	-
NGC5353	32±3	0.74±0.02	-12.48±0.01	4.39±0.10	0.17±0.03	1.1	283.5±4.8
NGC5532	73±6	0.97±0.02	-12.88±0.01	18.02±0.41	0.20±0.04	1.0	277.8±18.6
NGC5813	32±2	0.71±0.002	-11.33±0.001	43.88±0.10	0.45±0.01	2.5	235.4±3.4
NGC5846	34±6	0.79±0.003	-11.53±0.003	15.72±0.11	0.33±0.01	1.2	237.1±3.5
NGC5866	26±3	0.41±0.08	-13.05±0.02	0.33±0.02	0.5	1.1	161.6±4.8
NGC6098	108±12	1.60±0.11	-13.04±0.03	19.56±1.35	0.5	0.8	275.3±25.2
NGC6107	156±17	1.61±0.06	-12.66±0.02	46.30±2.13	0.58±0.14	1.0	240.9±28.1
NGC6251	130±23	0.83±0.03	-12.46±0.01	47.50±1.09	0.5	2.5	311.5±18.6
NGC6269	91±9	2.40±0.16	-12.51±0.01	84.64±1.95	1.01±0.27	1.1	317.9±22.4
NGC6278	27±3	2.05±0.30	-13.17±0.04	1.33±0.12	0.5	0.7	193.2±12.8
NGC6338	124±24	1.84±0.03	-11.80±0.004	264.49±2.44	0.84±0.07	1.2	348.4±40.2
NGC6482	37±4	0.82±0.007	-11.78±0.006	63.39±0.88	0.38±0.04	1.1	316.8±9.8
NGC6861	41±4	1.24±0.03	-12.50±0.01	6.24±0.14	0.17±0.03	1.1	406.9±19.6
NGC6868	62±5	0.75±0.02	-12.37±0.01	8.54±0.20	0.18±0.03	1.2	250.1±3.7
NGC7176	60±5	0.77±0.03	-12.79±0.02	2.51±0.12	0.5	1.0	245.9±5.7
NGC7196	39±3	0.64±0.04	-12.64±0.03	4.81±0.33	0.16±0.09	0.9	277.9±37.5
NGC7618	79±6	0.93±0.006	-12.05±0.004	59.50±0.55	0.25±0.02	1.3	292.8±30.3
NGC7626	52±3	0.93±0.02	-12.60±0.02	7.19±0.33	0.5	1.1	267.0±3.7
UGC408	57±4	0.82±0.01	-12.80±0.01	7.65±0.18	0.18±0.02	1.0	197.6±4.8


Figure 1. Comparisons of temperature (left panel) and X-ray luminosity (right panel) with previous works. The dashed line indicates the line of equality.

dust contribute to the absorption at higher N_H (Willingale et al. 2013). Thus, we also study the impact of Kalberla et al. (2005) N_H values (shown as second value in the last column of Table 1) on the best-fit spectral parameters. We found no significant influence of these new column density values on the derived temperatures and luminosities. The values for zero point, slope, and scatter are 0.05 ± 0.03 , 1.25 ± 0.19 , and 0.43 ± 0.07 , respectively. Moreover, we found that high N_H values produce higher uncertainties on the derived spectral parameters.

A small discrepancy was found between our X-ray luminosities and those from F06 and KF15. This discrepancy likely originates from differences in luminosity distances, D_L . Adopting the distances quoted in KF15, we obtain consistent luminosities for NGC1023, NGC3379, NGC3384, NGC4564, and NGC4621. However, the luminosity differences for NGC821, NGC4406, and NGC4486 are apparently not caused by differing luminosity distances. When the D_L quoted in KF15 are used to determine L_X from our measured fluxes, we obtain significantly different results. For instance, using the KF15 distances for NGC4406 gives a luminosity of 9.5×10^{40} erg/s, while KF15 quote 12.7×10^{40} erg/s. For this object, G16 and SI13 measured luminosities of 9.98 and 10.4×10^{40} erg/s, which is in agreement with our measurements.

4. MASS PROFILES

In this section we describe the derivation of the total and gas mass profiles. Studies have shown that the hot atmospheres of galaxies, groups, and clusters rest in hydrostatic equilibrium (Moore 1994; Churazov et al. 2008, 2010; Navarro et al. 2010; Babyk et al. 2014; Babyk 2016). Here we use a simple β -model (Cavaliere & Fusco-Femiano 1978) to describe the X-ray surface brightness profiles and to calculate total mass.

4.1. Surface brightness profile

The X-ray surface brightness profiles were extracted from the 0.5 – 6.0 keV X-ray images. Each profile contained 100 annular regions of uniform width, each centered on the X-ray peak. The radius of the outermost annulus, r_X , is distinct from the aperture used for the optical analysis. The X-ray SBPs were then fit with a single β -model:

$$S(r) = S_0 \left(1 + \left(\frac{r}{r_c} \right)^2 \right)^{-3\beta+1/2} + C, \quad (1)$$

where $S(r)$ is the X-ray surface brightness as a function of projected radius. S_0 , r_c , β , and C are free parameters in the model. We find that the SBPs of early-type galaxies are characterized by $\beta \approx 0.45 - 0.50$, which is smaller than the ~ 0.67 typical of galaxy clusters.

4.2. Total mass estimates

We derive the total gravitating mass for each galaxy assuming spherical symmetry and that the hot gas is in hydrostatic equilibrium. For gas in hydrostatic equilibrium,

$$\frac{dP}{dr} = -\frac{GM(r)}{r^2} \rho_g(r), \quad (2)$$

where P is the gas pressure, G is the gravitational constant, ρ_g is the gas density, and M is the total mass inside a sphere of radius r . The gas pressure is related to the gas density and

temperature through the ideal gas law, $P = \frac{\rho_g kT(r)}{\mu m_p}$. The total gravitating mass can then be written as

$$M(r) = -\frac{kT(r)r}{G\mu m_p} \left(\frac{d \ln \rho_g}{d \ln r} + \frac{d \ln T}{d \ln r} \right). \quad (3)$$

Here $\mu = 0.62$ is the mean molecular weight of the hot gas and m_p is the mass of a proton. Assuming that the gas is isothermal with mean temperature T , equation (3) becomes

$$M = -\frac{kTr}{G\mu m_p} \left(\frac{d \ln \rho_g}{d \ln r} \right). \quad (4)$$

The gas density profiles were determined using β -model fits to the X-ray surface brightness profiles. The gas density formulation for the β -model is

$$\rho_g(r) = \rho_0 \left(1 + \left(\frac{r}{r_c} \right)^2 \right)^{-3\beta/2}, \quad (5)$$

where r_c is the core radius and $\rho_0 = 2.21 \mu m_p n_0$ is the central gas density. The central concentration, n_0 , can be calculated from emissivity, ϵ , as

$$n_0 = \left[\frac{S_0}{r_c \epsilon B(3\beta - 0.5, 0.5)} \right]^{0.5}, \quad (6)$$

where $B(a, b)$ is the validity of the beta function (see Ettori (2000) for details). The total mass sampled range from 10^{12} to $10^{13} M_\odot$.

4.3. Gas mass estimates

The hot gas mass within a radius r_X was determined by integrating the gas density profiles (see Eq. 5):

$$M_g = 4\pi \rho_0 \int_0^{r_X} r^2 \left(1 + \left(\frac{r}{r_c} \right)^2 \right)^{-3\beta/2} dr. \quad (7)$$

The gas masses of our sampled elliptical and lenticular galaxies spans $10^9 - 10^{11} M_\odot$, while the gas masses of groups, BCGs, and cDs are an order of magnitude higher.

4.4. Summary of the calculations

The best-fitting parameters from the density formulation of the β -model are shown in Table 3. We present the gas and total masses measured within $5r_e$. When the X-ray surface brightness profile does not reach $5r_e$, we extrapolated the total and gas mass profiles out to $5r_e$ using the linear slope of the last 20 points in log-log space.

The main source of error in the gas mass are the modeled parameters β and r_c . The χ^2 values presented in Table 3 have not been divided by the degrees of freedom, 96. For most observations the β -model provides an accurate fit to the X-ray profile. We apply two methods to define the total mass uncertainties. First, we use the best-fitting parameters of β -model and Monte Carlo simulations. Due to the small uncertainties on β and r_c , the density and mass profiles have small statistical uncertainties. Second, we estimate the total mass uncertainties by propagating the errors through Eq. 4. The total mass uncertainties obtained from the best-fitting parameters are given as a second value in column 7 of Tab. 3, while propagated errors are given as a third value in the same column. We found that uncertainties obtained by the propagation method are higher by a factor of 1.5–2 than errors estimated from the best-fitting parameters.

Table 3
The best-fit parameters for an isothermal β -model.

Name	β	r_c kpc	ρ_0 10^{-24} g/cm ³	χ^2	M_g $10^{11} M_\odot$	M $10^{13} M_\odot$
(1)	(2)	(3)	(4)	(5)	(6)	(7)
ESO3060170	0.41±0.03	3.23±0.68	1.28±0.14	93	17.09±1.33	1.06±0.18±0.35
IC1262	0.57±0.04	27.3±2.27	0.25±0.05	217	38.6±3.7	1.40±0.20±0.42
IC1459	0.50±0.01	0.20±0.02	12.8±1.60	220	0.27±0.11	0.14±0.01±0.03
IC1633	0.63±0.02	1.88±0.15	3.37±0.40	243	4.63±0.45	1.70±0.08±0.21
IC4296	0.65±0.02	0.69±0.04	10.1±1.25	120	0.61±0.16	0.55±0.08±0.12
IC5267	0.37±0.02	0.18±0.01	2.71±0.30	120	0.44±0.12	0.08±0.01±0.03
IC5358	0.19±0.01	7.00±0.26	0.48±0.12	200	15.65±2.11	1.77±0.11±0.20
NGC315	0.53±0.01	0.79±0.04	6.77±0.72	108	2.72±0.65	0.38±0.02±0.05
NGC326	0.67±0.13	3.28±0.90	0.61±0.17	54	1.74±0.61	1.31±0.24±0.51
NGC383	0.90±0.13	2.88±0.07	1.74±0.15	160	0.18±0.03	0.52±0.02±0.04
NGC499	0.34±0.01	2.86±0.44	0.73±0.12	141	4.78±0.63	0.16±0.01±0.02
NGC507	0.35±0.01	0.47±0.07	3.57±0.39	178	6.96±0.54	0.52±0.01±0.02
NGC533	0.53±0.01	2.61±0.11	2.49±0.24	114	9.28±1.12	0.65±0.02±0.04
NGC708	0.35±0.01	2.69±0.06	1.70±0.21	462	18.10±2.64	0.49±0.01±0.02
NGC720	0.40±0.01	0.65±0.07	1.58±0.17	112	0.54±0.05	0.09±0.01±0.02
NGC741	0.46±0.01	1.09±0.09	0.33±0.05	161	5.96±0.73	0.43±0.02±0.04
NGC821	0.48±0.01	0.04±0.004	4.55±0.51	470	0.10±0.02	0.03±0.02±0.02
NGC1023	0.35±0.01	0.01±0.003	5.02±0.68	124	0.22±0.05	0.03±0.01±0.02
NGC1265	0.90±0.03	3.78±0.12	0.82±0.11	114	0.30±0.03	1.47±0.01±0.02
NGC1266	0.48±0.02	0.09±0.03	2.08±1.08	301	0.05±0.01	0.05±0.01±0.02
NGC1316	0.43±0.01	0.21±0.04	12.6±1.69	376	1.21±0.22	0.21±0.02±0.05
NGC1332	0.84±0.04	0.64±0.04	9.11±1.53	358	0.05±0.01	0.19±0.03±0.05
NGC1386	0.38±0.01	0.004±0.002	1.39±1.04	223	0.06±0.01	0.02±0.003±0.005
NGC1399	0.48±0.01	0.32±0.01	12.5±1.42	254	0.71±0.11	0.30±0.02±0.04
NGC1404	0.46±0.02	0.35±0.01	8.78±1.16	159	1.12±0.21	0.14±0.02±0.04
NGC1407	0.40±0.01	0.47±0.05	2.21±0.21	136	0.74±0.11	0.21±0.02±0.04
NGC1482	0.67±0.04	0.91±0.09	3.71±0.39	275	0.06±0.02	0.39±0.02±0.05
NGC1550	0.40±0.01	2.07±0.07	2.09±0.23	323	5.48±0.55	0.29±0.02±0.03
NGC1600	0.59±0.03	2.68±0.26	1.28±0.13	184	2.48±0.32	0.74±0.08±0.13
NGC1700	0.55±0.03	1.67±0.17	1.33±0.14	245	0.74±0.12	0.13±0.02±0.04
NGC2434	0.33±0.03	0.22±0.17	1.33±0.11	159	0.17±0.02	0.05±0.004±0.01
NGC2768	0.29±0.02	0.27±0.12	0.81±0.12	128	0.30±0.05	0.04±0.003±0.01
NGC3079	0.40±0.02	0.15±0.13	7.01±1.12	212	0.33±0.04	0.09±0.005±0.01
NGC3091	0.37±0.01	0.46±0.05	4.36±0.51	181	3.01±0.35	0.16±0.015±0.02
NGC3379	0.40±0.02	0.01±0.003	7.59±1.41	126	0.11±0.04	0.03±0.002±0.005
NGC3384	0.42±0.04	0.01±0.005	7.47±1.65	256	0.04±0.01	0.03±0.003±0.008
NGC3557	0.29±0.01	0.64±0.19	0.50±0.06	205	2.01±0.33	0.07±0.01±0.02
NGC3585	0.48±0.06	0.02±0.01	7.36±1.15	70	0.03±0.01	0.05±0.01±0.02
NGC3607	0.43±0.01	0.01±0.003	1.24±0.15	123	0.08±0.01	0.05±0.003±0.007
NGC3665	0.65±0.15	1.76±0.74	0.41±0.05	109	0.11±0.01	0.09±0.01±0.03
NGC3923	0.53±0.01	0.55±0.03	3.43±0.36	135	0.60±0.08	0.15±0.02±0.04
NGC3955	0.33±0.05	0.56±0.35	0.49±0.06	124	0.03±0.01	0.01±0.002±0.006
NGC4036	0.26±0.01	0.02±0.002	11.3±1.57	106	0.30±0.05	0.02±0.003±0.008
NGC4073	0.41±0.01	2.16±0.12	3.02±0.31	150	8.34±1.43	0.81±0.05±0.08
NGC4104	0.55±0.01	1.52±0.10	4.55±0.51	57	6.91±0.42	1.14±0.05±0.08
NGC4125	0.33±0.01	0.38±0.06	1.58±0.16	174	0.33±0.05	0.06±0.01±0.02
NGC4203	0.57±0.01	0.06±0.002	4.55±0.58	134	0.03±0.01	0.04±0.002±0.005
NGC4261	0.56±0.01	0.43±0.01	8.48±1.17	376	0.37±0.04	0.21±0.01±0.02
NGC4278	0.58±0.01	0.08±0.01	2.43±0.25	198	0.03±0.01	0.05±0.002±0.005
NGC4325	0.67±0.03	13.1±0.71	0.78±0.11	230	2.27±0.14	0.12±0.01±0.02
NGC4342	0.31±0.01	0.01±0.002	5.09±0.63	141	0.05±0.01	0.02±0.002±0.006
NGC4365	0.36±0.02	0.22±0.09	1.69±0.15	107	0.23±0.03	0.04±0.002±0.005
NGC4374	0.48±0.01	0.49±0.03	3.52±0.37	339	0.37±0.05	0.14±0.01±0.02
NGC4382	0.31±0.01	0.01±0.003	2.72±0.31	125	0.48±0.07	0.04±0.003±0.008
NGC4388	0.44±0.01	0.10±0.02	1.83±0.22	276	0.48±0.06	0.19±0.02±0.03
NGC4406	0.34±0.01	0.51±0.08	2.36±0.27	171	1.05±0.16	0.12±0.02±0.03
NGC4457	0.43±0.01	0.02±0.001	9.59±1.72	181	0.11±0.02	0.05±0.001±0.002

Table 3
Continued.

Name	β	r_c kpc	ρ_0 10^{-24} g/cm ³	χ^2	M_g $10^{11} M_\odot$	M $10^{13} M_\odot$
(1)	(2)	(3)	(4)	(5)	(6)	(7)
NGC4472	0.43±0.01	0.32±0.01	6.66±0.74	243	0.74±0.08	0.20±0.01±0.02
NGC4477	0.65±0.13	2.73±0.67	0.33±0.05	116	0.10±0.02	0.05±0.006±0.01
NGC4486	0.50±0.01	2.33±0.02	4.70±0.53	339	2.63±0.12	0.41±0.03±0.05
NGC4526	0.52±0.04	0.59±0.11	1.39±0.15	138	0.10±0.02	0.05±0.003±0.005
NGC4552	0.50±0.01	0.18±0.01	2.70±0.41	395	0.24±0.04	0.07±0.006±0.01
NGC4555	0.55±0.02	1.30±0.14	3.14±0.27	85	1.96±0.10	0.41±0.02±0.03
NGC4564	0.90±0.73	0.47±0.10	1.25±0.11	74	0.01±0.003	0.05±0.002±0.004
NGC4621	0.28±0.03	0.04±0.01	2.54±0.26	86	0.13±0.02	0.03±0.002±0.003
NGC4636	0.33±0.01	0.32±0.02	3.03±0.31	464	1.18±0.12	0.10±0.01±0.02
NGC4649	0.49±0.01	0.30±0.01	12.6±1.41	596	0.66±0.08	0.20±0.02±0.03
NGC4696	0.31±0.01	0.96±0.10	3.55±0.37	280	6.46±0.83	0.42±0.03±0.05
NGC4697	0.26±0.03	0.26±0.20	0.58±0.09	121	0.35±0.06	0.03±0.004±0.005
NGC4710	0.90±0.67	0.99±0.11	0.76±0.06	77	0.01±0.01	0.07±0.01±0.02
NGC4782	0.33±0.02	1.62±0.50	0.56±0.07	322	4.11±0.52	0.24±0.02±0.03
NGC4936	0.48±0.05	1.10±0.57	1.11±0.09	89	1.16±0.14	0.23±0.04±0.06
NGC5018	0.57±0.05	0.86±0.17	1.58±0.17	102	0.16±0.02	0.13±0.02±0.03
NGC5044	0.27±0.01	2.24±0.27	1.06±0.11	284	2.43±0.26	0.14±0.02±0.03
NGC5171	0.90±0.05	5.07±0.40	2.22±0.27	177	1.82±0.15	0.81±0.01±0.02
NGC5353	0.44±0.01	0.34±0.04	4.09±0.42	133	0.33±0.04	0.13±0.01±0.02
NGC5532	0.66±0.02	1.43±0.10	3.85±0.32	73	1.35±0.12	0.55±0.03±0.05
NGC5813	0.27±0.01	0.34±0.04	3.17±0.32	114	1.68±0.19	0.07±0.01±0.02
NGC5846	0.38±0.01	0.73±0.04	1.73±0.27	293	0.66±0.08	0.11±0.01±0.02
NGC5866	0.37±0.02	0.39±0.11	1.19±0.08	182	0.22±0.04	0.05±0.01±0.02
NGC6098	0.42±0.01	0.20±0.10	9.41±1.64	277	5.53±0.61	0.81±0.05±0.08
NGC6107	0.36±0.01	0.46±0.17	4.89±0.55	46	13.47±1.58	0.91±0.06±0.10
NGC6251	0.47±0.004	0.38±0.03	3.00±0.41	196	14.51±1.82	0.52±0.03±0.05
NGC6269	0.37±0.01	0.08±0.01	4.37±0.71	194	13.62±2.19	0.85±0.02±0.03
NGC6278	0.42±0.07	6.53±1.52	0.31±0.06	413	0.95±0.11	0.24±0.03±0.05
NGC6338	0.82±0.04	9.45±0.50	1.16±0.12	264	6.21±0.51	1.99±0.15±0.21
NGC6482	0.49±0.01	1.44±0.07	3.96±0.44	165	2.11±0.37	0.16±0.02±0.03
NGC6861	0.55±0.01	0.74±0.05	2.91±0.25	153	0.39±0.04	0.31±0.03±0.05
NGC6868	0.36±0.02	0.55±0.10	1.07±0.08	311	0.73±0.15	0.23±0.02±0.03
NGC7176	0.47±0.04	0.70±0.15	0.83±0.12	171	0.35±0.02	0.26±0.03±0.05
NGC7196	0.71±0.11	2.30±0.46	0.87±0.11	139	0.22±0.03	0.21±0.04±0.06
NGC7618	0.40±0.01	2.19±0.15	1.02±0.08	334	5.53±0.29	0.35±0.02±0.03
NGC7626	0.48±0.02	0.81±0.10	1.88±0.17	190	0.64±0.05	0.24±0.03±0.05
UGC408	0.90±0.68	1.54±0.13	1.11±0.10	64	0.03±0.01	0.51±0.02±0.03

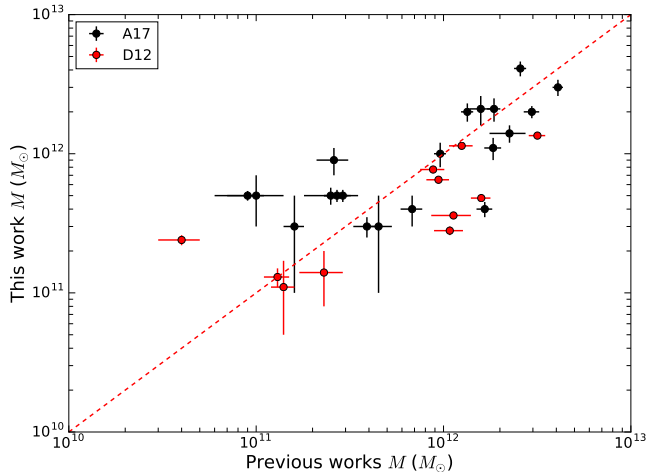


Figure 2. Comparison of total mass within $5r_e$ to previous works.

4.5. Comparison with previous results

In Figure 2 total mass measured within $5r_e$ is plotted against the total mass derived from stellar velocity dispersions. Velocity dispersions were obtained from Deason et al. (2012) and Alabi et al. (2017) (D12 and A17 in Figure 2, respectively). The dynamical measurements of total mass were also restricted to the central $5r_e$. D12 and A17 define their total early-type galaxy masses within $5r_e$ using the velocities of planetary nebulae and globular clusters. In general our masses agree with those from D12 and A17, although with large scatter for systems lying below $10^{12}M_\odot$. The principal source of error lies in the measurement of effective radius. Our effective radii are derived from optical data, while D12 and A17 use the near-IR. We explore this bias below.

Measurements of galaxy size are difficult to standardize because of their dependence on wavelength and background noise. As such, it is difficult to find a consensus on galaxy sizes in the literature, particularly at high stellar masses. For example, the SLUGGS sample (Alabi et al. 2016) used galaxy sizes taken from ATLAS^{3D}, which is based on 2MASS and RC3 estimates. These measurements underestimate galaxy sizes at high stellar masses by up to a factor 3 relative to the *Spitzer* masses from Forbes et al. (2016). The ATLAS^{3D} collaboration acknowledged this issue using the size-stellar mass relation. They found that the galaxies with high stellar masses are significantly smaller than expected (see Cappellari et al. 2011). Variations in effective radius naturally propagate into differences in mass measured at a fixed multiple of r_e . Deeper observations are better able to trace light in the outskirts of galaxies, enabling higher fidelity measurements of r_e . The *Spitzer* data are 3 magnitudes deeper than 2MASS, so are better suited for determining r_e . Additionally, the near-IR light observed by *Spitzer* traces old stars, where age and metallicity degeneracies are unimportant and effects of dust are minimized.

In Figure 3 we compare our optical effective radii to the near-IR radii measured by D12 and A17. Only 30 objects overlap. We therefore have repeated our measurement of r_e (see Sec. 2.1) using data from the *Spitzer* database, which includes 75 of our galaxies. We find general agreement between the optical and near-IR measurements for $r_e \geq 10$ kpc. At smaller r_e our optical radii are systematically larger than the near-IR values. We conclude that the large scatter seen in

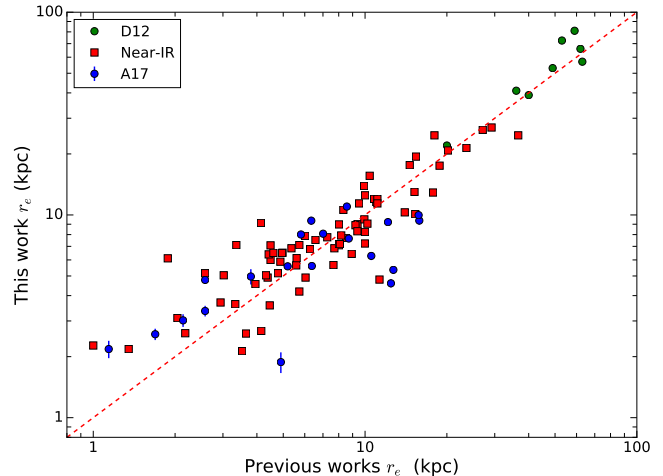


Figure 3. Comparison of effective radius estimates using optical *DSS* and near-IR *Spitzer* images to the radii defined in D12 and A17.

Fig. 2 for low masses is related to issues in the effective radius measurement.

5. SCALING RELATION RESULTS

In this section we explore four scaling relations for our sampled ETGs. In addition to the $L_X - T$, $M - T$, and $L_X - M$ relations, we derive the relation between total mass and $Y_X = T \times M_g$. The Y_X indicator has been studied primarily in galaxy clusters but not lower mass systems (Kravtsov et al. 2006; Nagai et al. 2007).

To determine the form of the scaling relation, we performed (1) linear fits in log space using the bivariate correlated error and intrinsic scatter (BCES) algorithm (Akritas & Ber-shady 1996) as well as (2) likelihood-based approach of Kelly (2007). The orthogonal BCES algorithm performs a linear least-squares regression that minimizes the orthogonal distance to the best-fit relation. Parameter uncertainties were determined using 10,000 Monte Carlo bootstrap re-samplings. Although the BCES method de-biases least squares linear regression for measurement errors, it is not perfect. Kelly’s regression is better, both in bias removal and in improved confidence intervals. It is a Bayesian method based on deriving a likelihood function. This method is implemented in Linmix package¹¹ and takes intrinsic scatter into account. Parameter uncertainties for Kelly’s methods were obtained by running $\sim 15,000$ steps of a Markov Chain Monte Carlo.

We find that both methods provide similar results. Since both these methods assume residuals are normally distributed, we perform the Anderson-Darling (AD) and Shapiro-Wilks (SW) tests to check their residuals for normality. We obtain $p > 0.5$ in our scaling relations, indicating that the residuals are normally distributed.

We also used the Pearson and Spearman correlation tests to determine the significance of linear relationship between two datasets. Finally we define a root mean square scatter (rms scatter) for each relation as

$$\text{rms} = \sqrt{\frac{\sum (f_i - \langle f \rangle)^2}{N}}, \quad (8)$$

where $\langle f \rangle$ is the fitted relation. This sample includes both gas-rich and gas-poor objects. We have therefore subdivided

¹¹ Python version - <https://github.com/jmeyers314/linmix>.

Table 4
Scaling relations of the form $\log(y) = a + b \log(x)$.

Sample	N	C_{cor}	a	b	p -Pearson	p -Spearman	p -AD	p -SW	rms scatter
$L_X - T$									
Full (BCES)	90	0.86	41.37 ± 0.07	4.42 ± 0.19	$\gg 0.0001$	$\gg 0.0001$	0.54	0.11	0.99
Full (Kelly's)	90	0.86	41.26 ± 0.07	4.53 ± 0.40	$\gg 0.0001$	$\gg 0.0001$	0.65	0.10	0.99
$L_X > 10^{40}$ (BCES)	65	0.75	43.15 ± 13.80	4.24 ± 0.16	$\gg 0.0001$	$\gg 0.0001$	0.55	0.28	0.67
$L_X > 10^{40}$ (Kelly's)	65	0.75	41.33 ± 0.06	3.78 ± 0.48	$\gg 0.0001$	$\gg 0.0001$	0.46	0.32	0.67
$L_X < 10^{40}$ (BCES)	25	0.60	40.95 ± 0.67	0.85 ± 1.24	0.0016	0.0016	0.74	0.08	0.38
$L_X < 10^{40}$ (Kelly's)	25	0.60	39.92 ± 0.26	1.09 ± 0.75	0.0016	0.0016	0.76	0.03	0.38
$M - T$									
Full (BCES)	90	0.85	12.56 ± 0.04	2.43 ± 0.19	$\gg 0.0001$	$\gg 0.0001$	0.35	0.29	0.52
Full (Kelly's)	90	0.85	12.47 ± 0.04	2.43 ± 0.25	$\gg 0.0001$	$\gg 0.0001$	0.38	0.43	0.52
$L_X - M$									
Full (BCES)	90	0.78	13.35 ± 2.34	2.78 ± 0.33	$\gg 0.0001$	$\gg 0.0001$	0.74	0.12	0.99
Full (Kelly's)	90	0.78	20.40 ± 1.95	2.65 ± 0.15	$\gg 0.0001$	$\gg 0.0001$	0.72	0.10	0.99
$M - Y_X$									
Full (BCES)	90	0.76	7.41 ± 0.41	0.45 ± 0.04	$\gg 0.0001$	$\gg 0.0001$	0.75	0.09	0.52
Full (Kelly's)	90	0.76	8.14 ± 0.49	0.38 ± 0.05	$\gg 0.0001$	$\gg 0.0001$	0.77	0.03	0.52

the sample based on X-ray luminosity. For consistency to previous works (e.g., [Kim & Fabbiano \(2013, 2015\)](#)), we set the L_X threshold at 10^{40} erg/s. The resulting best fits, their uncertainties, correlation coefficients, p -values for null-hypothesis and normality as well as rms scatters are shown in Table 4.

5.1. $L_X - T$

Our measured $L_X - T$ relation is shown on the left side of Figure 4. From top to bottom the relation is color-coded by galaxy type, metallicity, and stellar velocity dispersion. The contribution of LMXBs (green dashed line) and other faint stellar sources (magenta dashed line) to the total X-ray emission is shown in the upper left panel. These components were modeled simultaneously with the thermal emission described in Section 3. Our X-ray luminosity measurements for LMXBs and other stellar sources agree with previous estimates ([Irwin & Sarazin 1996, 1998](#); [Revnivtsev et al. 2007a,b](#); [Borson et al. 2011](#)). In addition, the X-ray luminosities of these components are consistent with expectations when scaling from stellar mass ([Revnivtsev et al. 2008a,b](#)). Using ROSAT observations, [Irwin & Sarazin \(1998\)](#) measured the X-ray luminosities of these stellar components to be in the range 10^{36} - 10^{39} erg/s. [Revnivtsev et al. \(2008a\)](#) found that the low-mass X-ray binaries are characterized by X-ray luminosities of 10^{37} - 10^{39} erg/s. In the 0.5-2.0 keV energy band, the unresolved X-ray emission is characterized by $L_X/M_* \sim 8.2 \times 10^{27}$ erg/s/ M_\odot (emissivity per unit stellar mass). It is consistent with measurements of dwarf ellipticals, spiral bulges, and the Milky Way. Such consistency suggests that the bulk of the unresolved emission is produced by an old stellar population that can be characterized by a universal emissivity per unit stellar mass (see [Revnivtsev et al. 2008a](#), for more details).

The best-fitting $L_X - T$ relations over our entire sample are $L_X \propto T^{4.42 \pm 0.19}$ and $L_X \propto T^{4.53 \pm 0.40}$ using BCES and Kelly's regression methods, respectively. For gas-rich objects with X-ray luminosities $> 10^{40}$ erg/s, the slopes are slightly shallower, 4.24 ± 0.16 and 3.78 ± 0.48 , respectively. Gas-poor objects below this value reveal no clear correlation. The metallicity and velocity dispersion subsamples are discussed further in the next section.

Our relation holds over a wide range of X-ray luminosity ($\sim 10^{38} - 5 \times 10^{42}$ erg/s) and temperature ($\sim 0.1 - 2$ keV). The most massive and luminous objects in our sample are BCGs

and cDs, which occupy top-right corner of the plot. The red dash-dotted line indicates the self-similar scaling. Our observed $L_X - T$ relation is significantly steeper than the self-similar prediction of $L_X \propto T^2$. This steepening indicates baryonic physics on both small and large scales. The $L_X - T$ relation is steeper in ETGs than in clusters, indicating that non-gravitational processes are more efficient in low-mass systems.

5.2. $M - T$

We have investigated the $M - T$ relation of ETGs in a sample of 90 systems. The right-hand plots in Figure 4 show the $M - T$ relation, with color coding the same as in Section 5.1. The best-fit results are $M \propto T^{2.43 \pm 0.19}$ for BCES and $M \propto T^{2.43 \pm 0.25}$ for Kelly's, respectively, with an rms deviation of 0.52 dex. According to the self-similar model, the total mass should scale with temperature as $M \propto T^{3/2}$. Thus, this relation is also significantly steeper than is predicted by self-similarity. The main contributors to this steepening are galaxies with temperatures below 0.7 keV. Fitting only galaxies with $kT < 0.7$ keV we find a steeper relation, with $M \propto T^{3.2 \pm 0.4}$.

Most of the X-ray flux emerges from the centers of galaxies. Therefore, the $L_X - T$ scaling relation shows larger scatter compared to the $M - T$ relation, consistent with previous results for galaxy clusters ([Markevitch et al. 1998](#); [Arnaud & Evrard 1999](#); [Pratt et al. 2009](#); [Maughan et al. 2012](#)). Thus, the total mass-temperature relation is less sensitive to the non-gravitational processes.

5.3. $L_X - M$

The scaling relations between X-ray luminosity and total mass are shown on the left-hand side of Figure 5. For the entire sample we measured $L_X \propto M^{2.78 \pm 0.23}$ and $L_X \propto M^{2.65 \pm 0.15}$, for BCES and Kelly's methods respectively. Due to the high scatter in high-mass systems (mostly BCGs and cDs), the slope has relatively large uncertainty.

Furthermore, Malmquist bias is present in both the $L_X - T$ and $L_X - M$ scaling relations ([Staneke et al. 2006](#); [Vikhlinin et al. 2009](#); [Main et al. 2017](#)). This bias can be quantified by $\delta \ln L_X = 3/2 \sigma_i^2$, where σ_i is an intrinsic scatter in the log-normal value of luminosity for a given T . We correct for this bias to our $L_X - T$ and $L_X - M$ relations, modifying the nor-

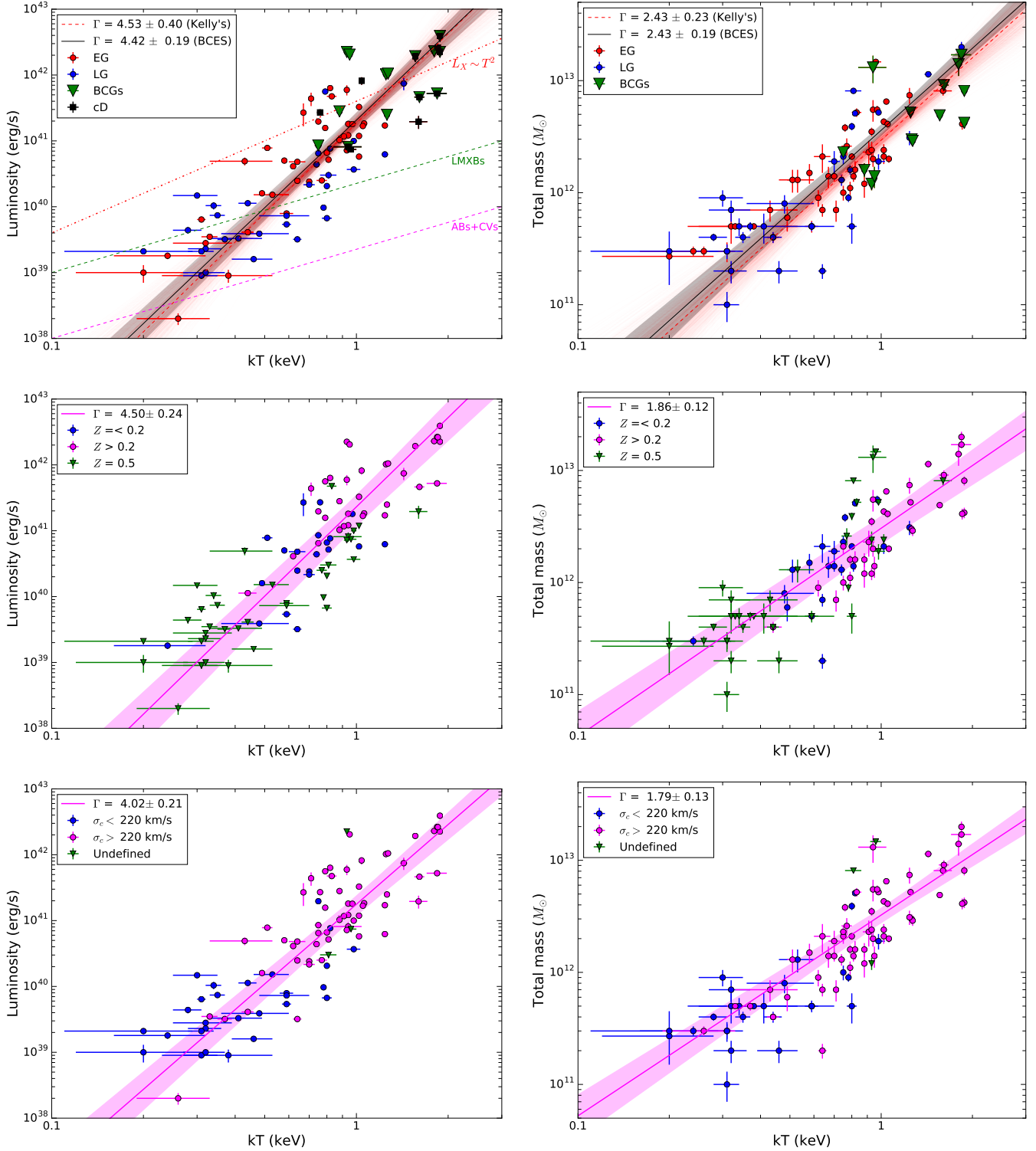


Figure 4. The relations between X-ray luminosity (left) and total mass (right) with temperature, each derived within $5r_e$. The solid black and dashed red lines indicate the best-fitting relation for the entire ETG sample using BCES and Kelly's regression methods. In the upper left plot the red dashed-dotted line indicates the self-similar $L_X \sim T^2$ relation, and the green and magenta dashed lines show the contributions to the total X-ray luminosity from LMXBs and other stellar sources. The shaded regions in all panels indicate the 1σ confidence levels for the fitted scaling relations. The subsamples in each row are color-coded by morphological type (top), metallicity (middle), and σ_c -fast/slow (bottom). The power laws shown in magenta were BCES fit with the gas-rich (middle) and σ_c -fast (bottom) galaxies only.

Table 5
Comparison with previous X-ray scaling relation measurements.

Our results	Literature	Ref
$L_X - T$		
	$L_X \propto T^{4.8 \pm 0.7}$	O’Sullivan et al. (2003)
$L_X \propto T^{4.4 \pm 0.2}$ (BCES)	$L_X \propto T^{4.6 \pm 0.7}$	Boroson et al. (2011)
$L_X \propto T^{4.5 \pm 0.4}$ (Kelly’s)	$L_X \propto T^{4.5 \pm 0.3}$	Kim & Fabbiano (2015)
	$L_X \propto T^{4.7 \pm 0.4}$	Goulding et al. (2016)
$L_X - M$		
$L \propto M^{2.8 \pm 0.3}$ (BCES)	$L_X \propto M^{2.7 \pm 0.3}$	Kim & Fabbiano (2013)
$L \propto M^{2.7 \pm 0.2}$ (Kelly’s)	$L_X \propto M^{3.13 \pm 0.32}$	Forbes et al. (2016)

malization of our fit but not the power law slope involving L_X .

5.4. $M - Y_X$

The total mass – Y_X scaling relation was initially investigated in galaxy clusters by Kravtsov et al. (2006). Here we explore for the first time this relation in ETGs. The $M - Y_X$ relation is shown on the right-hand side of Figure 5. We find a strong positive correlation with best-fitting power law scaling $M \propto Y_X^{0.45 \pm 0.04}$ (BCES) and rms deviation of 0.52 dex. Using Kelly’s regression method we find a slightly shallower scaling relation, $M \propto Y_X^{0.38 \pm 0.05}$. Both slopes are shallower than the slope of 3/5 measured in clusters alone (Kravtsov et al. 2006, referred to as KVN). The dashed red line in the top-right plot of Fig. 5 shows the scaling measured by KVN for their sample of relaxed galaxy clusters.

5.5. Comparison with previous results

In Table 5 we compare our results to previously published X-ray scaling relations for ETGs (O’Sullivan et al. 2003; Boroson et al. 2011; Kim & Fabbiano 2013, 2015; Goulding et al. 2016; Forbes et al. 2016). Our results are consistent with but have lower uncertainties than these studies. O’Sullivan et al. (2003) performed their $L_X - T$ scaling relation analysis for a sample of cD galaxies. Later, Kim & Fabbiano (2015) found a significantly steeper $L_X - T$ relation ($L_X \propto T^{5.4 \pm 0.6}$) for their sample, which included cD galaxies as well. Boroson et al. (2011) found that the gas-poor ETGs follow the power law fit $L_X \propto T^{4.5 \pm 0.55}$. However, David et al. (2006) found no clear correlation between X-ray luminosity and temperature for a sample of 18 gas-poor ETGs.

The X-ray $L_X - M$ relation of 14 ETGs has been investigated by Kim & Fabbiano (2013). They found the scatter in gas-poor objects ($L_X \lesssim 3 \times 10^{39}$ erg/s) to be larger than in gas-rich galaxies. Forbes et al. (2016) presented a strong correlation between X-ray luminosity and galaxy dynamical mass within $5r_e$ for a sample of 29 massive ETGs obtained using the SLUGGS survey.

6. DISCUSSION

Here we use X-ray scaling relations to explore the structural and dynamical properties of ETGs. We first subdivided our sample on metallicity, stellar velocity dispersion, and X-ray core size. The stellar velocity dispersion threshold was chosen to be 220 km/s for consistency with previous results. For metallicity and X-ray core size we have built histograms of metallicity and core radius. The peaks were chosen as our thresholds. Due to the similarity of best-fitting results for scaling relations analyzed in the previous section with BCES and Kelly’s methods, further fitting has been performed with the

BCES method only. The best-fitting relations for each subsample are shown in Table 6. We found no clear correlations in the $M - Y_X$ scaling relation for the subdivided samples.

We find that more massive galaxies are characterized by a higher metallicity, higher central velocity dispersions, and larger X-ray cores. We also explore the gas-to-total mass fraction and the $L_X - \sigma_c$ relation. Finally, we explore whether AGN feedback causes the X-ray scaling relations to deviate from self-similarity.

6.1. Metallicity in ETGs

Atmospheric metallicity is sensitive to several physical processes, including star formation history and outflows. The stars in massive galaxies are metal-rich compared to lower mass galaxies. Due to their shallower gravitational potential wells, lower mass galaxies are more easily stripped of enriched gas (Faber 1973; Babyk & Vavilova 2012).

Using the metallicities measured from spectral fitting in Table 2, we subdivided our sample into metal-rich and metal-poor systems. A metallicity of $0.2 Z_\odot$ divided the sample. The middle panels in Figures 4 and 5 show the metal-rich and metal-poor subsamples in each scaling relation. We find a strong, steep $L_X - T$ correlation for metal-rich ($Z > 0.2 Z_\odot$) galaxies with an rms deviation of 0.59. Metal-poor galaxies ($Z < 0.2 Z_\odot$), on the other hand, show a weak $L_X - T$ relation that is shallower than the metal-rich $L_X - T$ relation. The $M - T$ relation is strongly correlated for metal-rich galaxies, while the $L_X - M$ and $M - Y_X$ relations have significantly higher scatter.

Galaxies with temperatures lying between 0.5 and 1.0 keV are usually degenerate in metallicity, temperature and normalization of the thermal model (Werner et al. 2012). Werner et al. (2012) found that overestimating metallicity by a factor of two will underestimate the normalization by a factor of ~ 1.35 . To explore the effect on our scaling relations, we fit the most metal-rich and metal-poor objects with a fixed metallicity that varied between 0.1 and $1.0 Z_\odot$ in steps of $0.1 Z_\odot$. We found that objects with temperatures $\lesssim 1.2$ keV were not affected by metallicity variations. The sources with temperature $\gtrsim 1.2$ keV correlate with metallicity. A mis-estimate of metallicity of this size has a relatively small impact on X-ray luminosity.

6.2. σ_c -fast/slow galaxies

We investigated the gross dynamical properties of ETGs using their central velocity dispersions. We divided our sample into σ_c -fast and slow objects using a threshold of $\sigma_c = 220$ km s $^{-1}$, following Kim & Fabbiano (2015). These subsamples are highlighted in the bottom panels of Figures 4 and 5. The $L_X - T$ and $M - T$ relations both show strong correlations for σ_c -fast galaxies. Galaxies with higher central velocity dispersions are hotter, more luminous, and are more massive (in both total and gas mass) than those with lower velocities.

6.3. X-ray core/coreless galaxies

To explore the relationship between stellar cores and atmospheric cores we subdivide our sample using the core radius r_c obtained from the β -model fit to the X-ray surface brightness profiles. A significant X-ray core corresponds to systems with $r_c > 0.5$ kpc, while coreless galaxies have $r_c < 0.5$ kpc. All four scaling relations, color-coded by the presence or not of an X-ray core, are shown in Figure 6. The power law fits

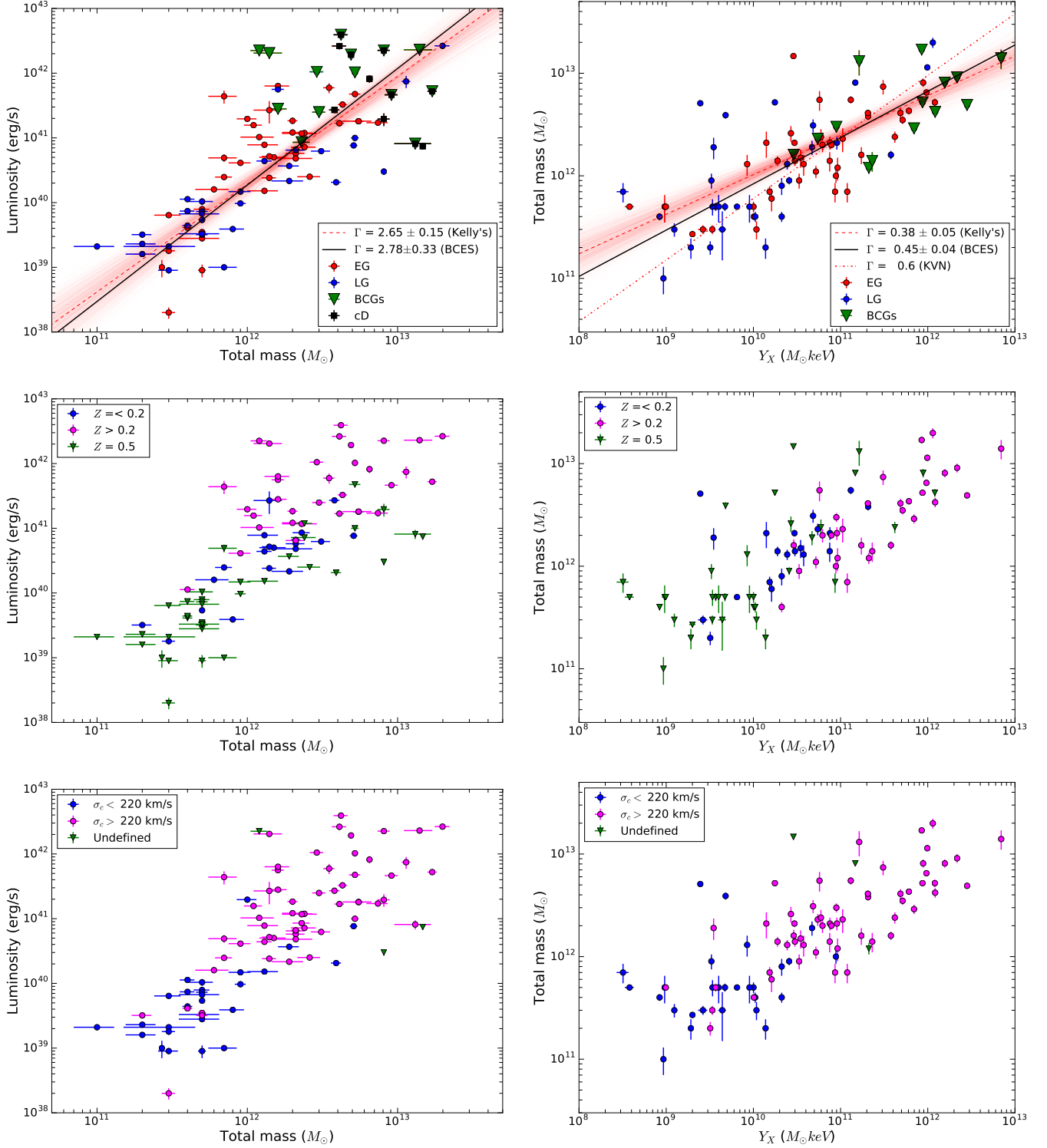


Figure 5. The X-ray luminosity – total mass (left) and total mass – Y_X (right) relations for the entire ETG sample. The solid black and dashed red lines indicate the best-fitting relation for the entire ETG sample using BCES and Kelly’s regression methods. The red dash-dotted line shows the best-fitting result from Kravtsov et al. (2006) obtained for galaxy clusters. The color-coding in each row is the same as in Fig. 4.

Table 6
Scaling relations of the form $\log(y) = a + b \log(x)$. Luminosities are expressed in units of 10^{40} erg/s and masses in $10^{12} M_{\odot}$.

Sample	N	C_{cor}	a	b	p -Pearson	p -Spearman	rms scatter
$L_X - T$							
X-ray core	42	0.84	56.08 ± 22.27	4.46 ± 0.23	$\gg 0.0001$	$\gg 0.0001$	0.90
X-ray coreless	35	0.83	8.93 ± 3.82	2.87 ± 0.55	$\gg 0.0001$	$\gg 0.0001$	0.92
Z-rich	33	0.75	76.82 ± 36.46	4.50 ± 0.24	$\gg 0.0001$	$\gg 0.0001$	0.59
Z-poor	21	0.64	8.57 ± 4.59	1.68 ± 0.44	0.0016	0.0033	0.59
σ_c -fast	59	0.82	35.42 ± 11.07	4.02 ± 0.21	$\gg 0.0001$	$\gg 0.0001$	0.83
σ_c -slow	28	0.70	3.42 ± 2.06	1.79 ± 0.89	$\gg 0.0001$	0.00025	0.57
$M - T$							
X-ray core	42	0.78	9.52 ± 1.50	1.86 ± 0.12	$\gg 0.0001$	$\gg 0.0001$	0.43
X-ray coreless	35	0.85	2.52 ± 0.36	1.99 ± 0.82	$\gg 0.0001$	$\gg 0.0001$	0.47
Z-rich	33	0.86	3.05 ± 0.81	1.86 ± 0.20	$\gg 0.0001$	$\gg 0.0001$	0.41
Z-poor	21	0.69	3.34 ± 1.25	2.64 ± 0.40	0.0005	$\gg 0.0001$	0.36
σ_c -fast	59	0.83	3.28 ± 0.44	1.79 ± 0.13	$\gg 0.0001$	$\gg 0.0001$	0.43
σ_c -slow	28	0.68	1.97 ± 0.53	1.61 ± 0.43	$\gg 0.0001$	$\gg 0.0001$	0.36
$L_X - M$							
X-ray core	42	0.90	5.37 ± 0.17	0.06 ± 0.33	$\gg 0.0001$	0.0005	0.92
X-ray coreless	35	0.86	3.28 ± 0.13	1.63 ± 0.46	$\gg 0.0001$	$\gg 0.0001$	0.92
Z-rich	33	0.53	3.53 ± 0.13	0.43 ± 0.42	0.0014	0.047	0.59
Z-poor	21	0.83	2.05 ± 0.77	1.14 ± 0.45	$\gg 0.0001$	$\gg 0.0001$	0.59
σ_c -fast	59	0.72	4.49 ± 1.15	0.78 ± 0.30	$\gg 0.0001$	$\gg 0.0001$	0.83
σ_c -slow	28	0.70	1.04 ± 0.64	1.03 ± 0.65	$\gg 0.0001$	$\gg 0.0001$	0.56

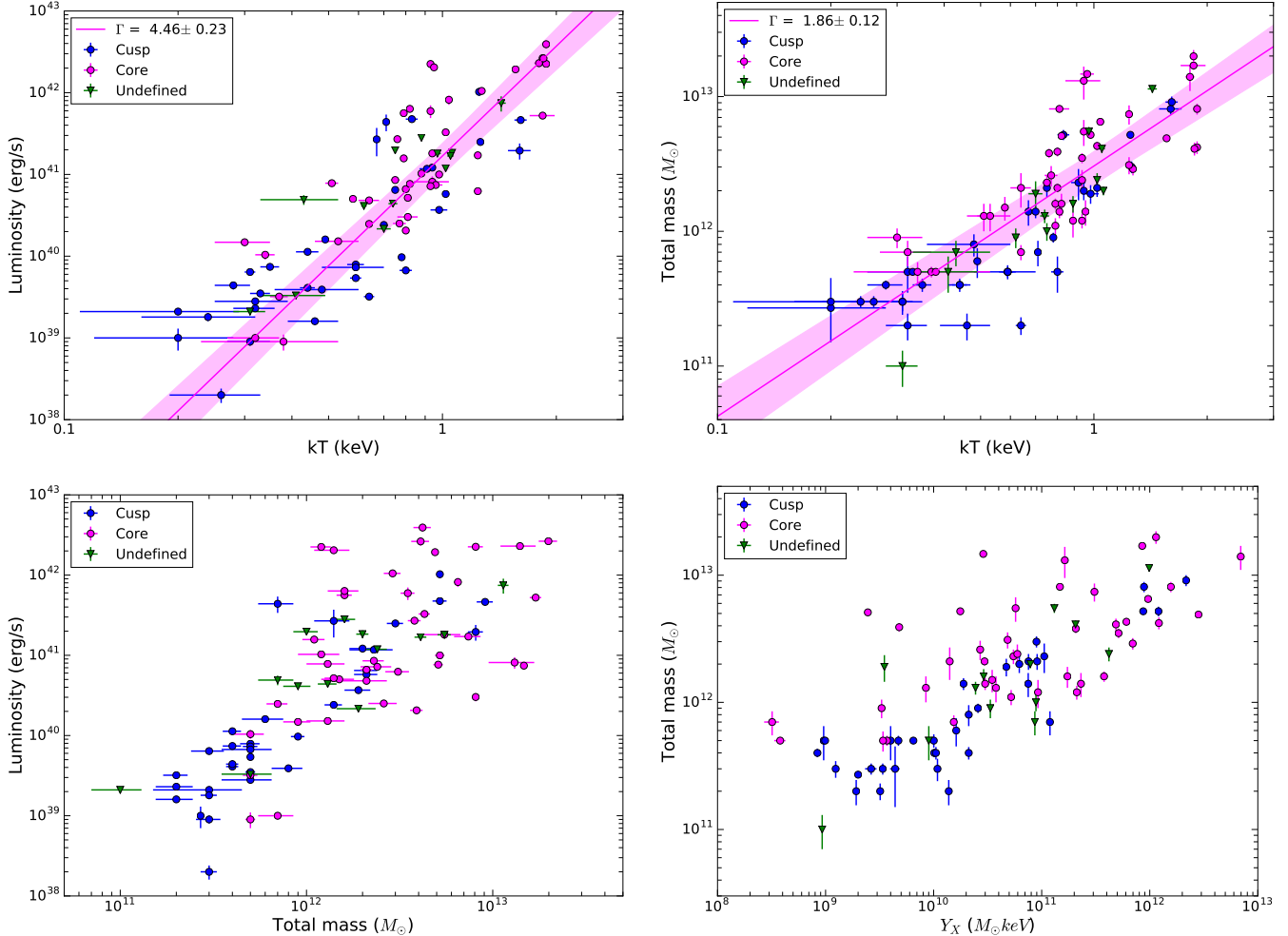


Figure 6. The X-ray scaling relations for galaxies with an X-ray core/cusp. The fits in magenta were obtained from X-ray core galaxies only.

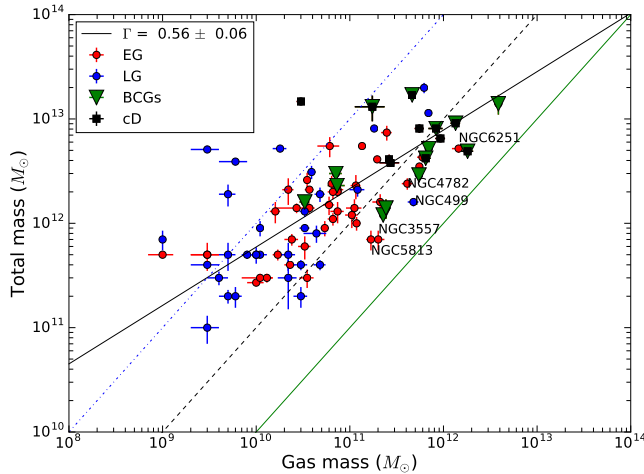


Figure 7. The relation between total mass and gas mass, both derived within $5r_e$. The solid, dashed, and dash-dotted lines correspond to gas fractions of 1, 0.1, and 0.01, respectively.

to the subsamples are given in Table 6. No clear separation between X-ray core and coreless galaxies in temperature, luminosity, and mass is found.

6.4. The $M_g - M$ relation

The relationship between total mass and atmospheric mass is shown in Figure 7. The dash-dotted, dashed and solid lines correspond to constant gas-to-total mass fractions of 0.01, 0.1, and 1. We observe a weak correlation, $M \propto M_g^{0.56 \pm 0.06}$, spanning 4 decades in atmospheric mass and ~ 2 decades in total mass. The total masses of BCGs and cD galaxies are similar at roughly $10^{12} M_\odot$. The gas fraction in lenticular galaxies is lower than that in elliptical galaxies. The gas fractions in elliptical and lenticular galaxies lie below ~ 0.1 . Only 5 ETGs (those labeled in Figure 7), apart from BCGs and cDs, have gas fractions above 0.1.

6.5. The $L_X - \sigma_c$ relation

The X-ray luminosity of a virialized, self-similar atmosphere should scale with stellar velocity dispersion as $L_X \propto \sigma_c^4$. Recent observations of galaxy clusters give steeper slopes, e.g., $L_X \propto \sigma_c^{5.2 \pm 0.3}$ (Wu et al. 1999). Steep $L_X - \sigma_c$ relations for elliptical galaxies $L_X \propto \sigma_c^{8-11}$, have been found (Diehl & Statler 2007; Goulding et al. 2016). We find $L_X \propto \sigma_c^{5.16 \pm 0.53}$ for the entire sample, Figure 8. Including ellipticals only steepens the relationship to $L_X \propto \sigma_c^{12.6 \pm 1.9}$, consistent with observational results of Goulding et al. (2016) and cosmological simulations of Davé et al. (2002).

6.6. Impact of AGN feedback

The slopes of the X-ray scaling relations are steeper than self-similar scaling. Departures from self-similarity indicate extra thermal processes acting on the atmospheres of early-type galaxies (Giodini et al. 2013). The effects increase significantly from clusters to the lower mass atmospheres of groups and galaxies. Heat sources capable of driving the scaling away from self-similarity include supernovae feedback, stellar mass loss, thermal conduction, cosmic rays, and AGN feedback. Each of these contributes at a level that varies with the mass of the system. However, the impact of any individual process on a hot atmosphere is poorly known. AGN

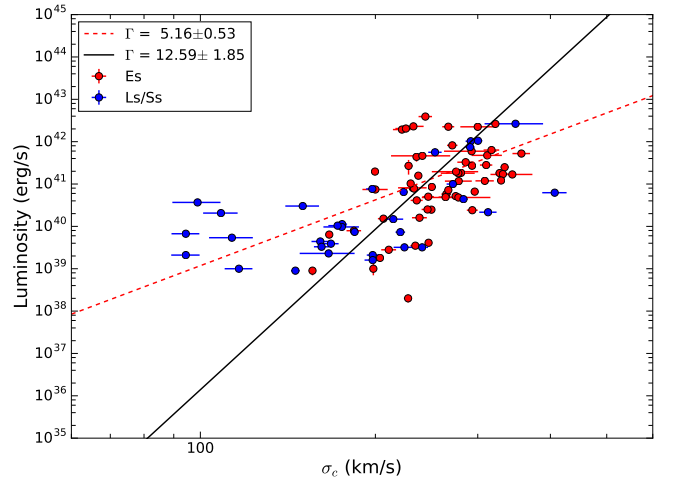


Figure 8. The relation between X-ray luminosity and central velocity dispersion.

feedback is the largest heat source that is prevalent across all masses (Anderson et al. 2015a; Main et al. 2017; Pellegrini et al. 2012; McNamara & Nulsen 2007, 2012). The departures from self-similarity of the X-ray scaling relations of clusters, groups, and galaxies can be largely attributed to AGN feedback, which we discuss briefly below.

Puchwein et al. (2008) performed hydrodynamic simulations that included radiative cooling, star formation, supernova feedback, and heating by the ultraviolet background. Their simulations have been applied to the systems with and without black hole growth (Sijacki et al. 2007). Without AGN heating, the X-ray luminosities of poor clusters and galaxies with $kT \leq 2-3$ keV are overestimated. This result agrees with earlier studies (e.g. Borgani et al. 2004; Khosroshahi et al. 2004; Sijacki & Springel 2006; Nagai et al. 2007; Schaye et al. 2010; Gaspari et al. 2012, 2014; Anderson et al. 2015a,b). Their simulated $L_X - T$ scaling relation also agrees with our observations of massive clusters and groups. The models imply that AGN feedback removes hot gas from the cores of poor clusters and groups, suppressing the X-ray luminosity and thus steepening the $L_X - T$ relation. The $L_X - T$ scaling relation obtained by Puchwein et al. (2008) agrees with observations over a wide range of mass scales, from massive clusters to small groups.

The influence of AGN feedback on the $L_X - T$ scaling relation of ellipticals has been recently studied by Gaspari et al. (2012, 2014). They used two feedback prescriptions: a quasar thermal blast and self-regulated kinetic feedback. Their hydrodynamic simulations include stellar evolution and cooling over the life of the galaxy. They successfully reproduced observed properties, including buoyant cavities, subsonic turbulence, and nuclear cold gas. They argued that AGN feedback in isolated galaxies should be both less efficient and powerful compared to ellipticals because the latter are influenced by gas in the intergalactic medium. They also concluded that both AGN feedback models describe well the observational $L_X - T$ scaling relation. However, the decreasing X-ray luminosity below ~ 0.5 keV in the model is not evident in our scaling relations. In other words, we do not observe a break in the $L_X - T$ relation. We observe a monotonically decreasing X-ray luminosity in the $L_X - T$ and $L_X - M$ relations toward the lower temperatures (~ 0.2 keV). This feature is reproduced by a gentle, self-regulated kinetic mechanism (An-

derson et al. 2015a,b). Recently, Negri et al. (2014) predicted higher temperatures in low luminosity systems than we and Kim & Fabbiano (2015) observe.

The effects of AGN winds and radiation on the temperatures and X-ray luminosities of elliptical galaxies were modeled using high-resolution, 1D hydrodynamical simulations (Pellegrini et al. 2012). Their simulations produce the large variations in L_X observed in our sample. In addition, Choi et al. (2015) performed a set of particle hydrodynamic simulations, adding a pressure-entropy formulation to improve fluid mixing and the treatment of contact gaps. These simulations have been applied to 20 haloes with AGN feedback models that included no feedback, thermal feedback, and radiation and mechanical feedback. The feedback models successfully reproduced the $M_{BH} - \sigma$ relation. They found that X-ray luminosity is determined primarily by galaxy mass, consistent with our $L_X - M$ scaling relation.

Davé et al. (2002) examined the scaling of temperature, X-ray luminosity, and galaxy velocity dispersion for a sample of galaxy groups. They used a Λ CDM simulation that included prescriptions for gas dynamics, star formation, radiative cooling, and gravity. In agreement with our results, their $L_X - \sigma$ and $L_X - T$ relations steepen below $kT \approx 0.7$ keV and $\sigma \approx 180$ km/s. They argued that the breaks result from the increasing efficiency of radiative cooling in low-mass systems. Cooling affects both the density and the hot gas fraction.

It is clear that a deeper understanding of AGN feedback is required. Unfortunately, a complete theoretical picture of AGN feedback is still under debate. The current theoretical models need improvements with a new input physics and our scaling relations can be easily used for comparison with a new generation of simulations.

7. CONCLUSIONS

We derived atmospheric temperature, density, gas masses, and total masses for 94 early type galaxies using archival *Chandra* observations. We derived X-ray scaling relations for the largest sample of ETGs to date. The main results and conclusions can be summarized as follows.

- We derived X-ray scaling relations between luminosity, temperature, mass, and Y_X . We find $L_X \propto T^{4.42 \pm 0.19}$, $M \propto T^{2.43 \pm 0.19}$, $L_X \propto M^{2.78 \pm 0.33}$, $M \propto Y_X^{0.45 \pm 0.04}$.
- Our results are significantly steeper than self-similar expectations. The steepening of the relations is likely due to AGN feedback. The tight $L_X - T$ correlation for low-luminosities systems (i.e., below 10^{40} erg/s) are at variance with hydrodynamical simulations which generally predict higher temperatures for low luminosity galaxies.
- We investigated the structural and dynamical properties of ETGs over a wide range of temperature (0.2 – 2.0 keV), X-ray luminosity ($10^{38} - 10^{43}$ erg/s), and total mass ($10^{12} - 10^{13} M_\odot$). We found no correlation between the gas-to-total mass fraction with temperature or total mass.

BRM acknowledges funding from the Natural Sciences and Engineering Research Council of Canada, the University of Waterloo's Faculty of Science, and the Perimeter Institute. ACE acknowledges support from STFC grant ST/P00541/1.

We thank A. Alabi for useful discussions related to the effective radius measurements, and K. Arnaud for comments related to spectral modeling. This research has made use of data obtained from the Chandra Data Archive and the Chandra Source Catalog, and software provided by the Chandra X-ray Center (CXC) in the application packages CIAO, ChIPS, and Sherpa. We thank all the staff members involved in the Chandra project. This research has made use of the NASA/IPAC Extragalactic (NED), SIMBAD, and LEDA databases. We also thank all members involved into the *DSS* and *Spitzer* collaborations. Additionally we have used ADS facilities.

REFERENCES

- Akritas, M. G., & Bershady, M. A. 1996, *ApJ*, 470, 706
- Alabi, A. B., Forbes, D. A., Romanowsky, A. J., et al. 2016, *MNRAS*, 460, 3838
- . 2017, ArXiv e-prints, arXiv:1701.05904
- Anderson, M. E., Gaspari, M., White, S. D. M., Wang, W., & Dai, X. 2015a, *MNRAS*, 449, 3806
- . 2015b, *MNRAS*, 449, 3806
- Arnaud, K. A. 1996, in *Astronomical Society of the Pacific Conference Series*, Vol. 101, *Astronomical Data Analysis Software and Systems V*, ed. G. H. Jacoby & J. Barnes, 17
- Arnaud, M., & Evrard, A. E. 1999, *MNRAS*, 305, 631
- Babyk, I. 2016, *Astronomy Reports*, 60, 542
- Babyk, I., & Vavilova, I. 2014, *Ap&SS*, 349, 415
- Babyk, I. V., Del Popolo, A., & Vavilova, I. B. 2014, *Astronomy Reports*, 58, 587
- Babyk, I. V., & Vavilova, I. B. 2012, *Odessa Astronomical Publications*, 25, 119
- Bender, R., Surma, P., Doebereiner, S., Moellenhoff, C., & Madejsky, R. 1989, *A&A*, 217, 35
- Beuing, J., Doebereiner, S., Bohringer, H., & Bender, R. 1999, *MNRAS*, 302, 209
- Birzan, L., Rafferty, D. A., McNamara, B. R., Wise, M. W., & Nulsen, P. E. J. 2004, *ApJ*, 607, 800
- Booth, C. M., & Schaye, J. 2010, *MNRAS*, 405, L1
- Borgani, S., Finoguenov, A., Kay, S. T., et al. 2005, *MNRAS*, 361, 233
- Borgani, S., & Viel, M. 2009, *MNRAS*, 392, L26
- Borgani, S., Murante, G., Springel, V., et al. 2004, *MNRAS*, 348, 1078
- Borgani, S., Dolag, K., Murante, G., et al. 2006, *MNRAS*, 367, 1641
- Boroson, B., Kim, D.-W., & Fabbiano, G. 2011, *ApJ*, 729, 12
- Bryan, G. L., & Norman, M. L. 1998, *ApJ*, 495, 80
- Cappellari, M., Emsellem, E., Krajnovic, D., et al. 2011, *MNRAS*, 413, 813
- Cash, W. 1979, *ApJ*, 228, 939
- Cavaliere, A., & Fusco-Femiano, R. 1978, *A&A*, 70, 677
- Choi, E., Ostriker, J. P., Naab, T., Oser, L., & Moster, B. P. 2015, *MNRAS*, 449, 4105
- Churazov, E., Forman, W., Vikhlinin, A., et al. 2008, *MNRAS*, 388, 1062
- Churazov, E., Tremaine, S., Forman, W., et al. 2010, *MNRAS*, 404, 1165
- Davé, R., Katz, N., & Weinberg, D. H. 2002, *ApJ*, 579, 23
- David, L. P., Forman, W., & Jones, C. 1991, *ApJ*, 369, 121
- David, L. P., Jones, C., Forman, W., Vargas, I. M., & Nulsen, P. 2006, *ApJ*, 653, 207
- Deason, A. J., Belokurov, V., Evans, N. W., & McCarthy, I. G. 2012, *ApJ*, 748, 2
- Dickey, J. M., & Lockman, F. J. 1990, *ARA&A*, 28, 215
- Diehl, S., & Statler, T. S. 2007, *ApJ*, 668, 150
- Ettori, S. 2000, *MNRAS*, 318, 1041
- Evrard, A. E., Metzler, C. A., & Navarro, J. F. 1996, *ApJ*, 469, 494
- Fabbiano, G. 1989, *ARA&A*, 27, 87
- Faber, S. M. 1973, *ApJ*, 179, 423
- Fabian, A. C., Walker, S. A., Russell, H. R., et al. 2017, *MNRAS*, 464, L1
- Forbes, D. A., Alabi, A., Romanowsky, A. J., et al. 2016, *MNRAS*, 458, L44
- Forman, W., Churazov, E., Jones, C., et al. 2017, *ApJ*, 844, 122
- Fukazawa, Y., Botoya-Nonesca, J. G., Pu, J., Ohto, A., & Kawano, N. 2006, *ApJ*, 636, 698
- Gaspari, M., Brighenti, F., & Temi, P. 2012, *MNRAS*, 424, 190
- Gaspari, M., Brighenti, F., Temi, P., & Ettori, S. 2014, *ApJ*, 783, L10
- Godini, S., Lovisari, L., Pointecouteau, E., et al. 2013, *Space Sci. Rev.*, 177, 247
- Goulding, A. D., Greene, J. E., Ma, C.-P., et al. 2016, *ApJ*, 826, 167
- Hlavacek-Larrondo, J., McDonald, M., Benson, B. A., Forman, W. R., & Allen, S. W. 2015, *ApJ*, 805, 35

- Irwin, J. A., & Sarazin, C. L. 1996, *ApJ*, 471, 683
 —. 1998, *ApJ*, 494, L33
 Kaiser, N. 1986, *MNRAS*, 222, 323
 Kalberla, P. M. W., Burton, W. B., Hartmann, D., et al. 2005, *A&A*, 440, 775
 Kelly, B. C. 2007, *ApJ*, 665, 1489
 Khosroshahi, H. G., Raychaudhury, S., Ponman, T. J., Miles, T. A., & Forbes, D. A. 2004, *MNRAS*, 349, 527
 Kim, D.-W., & Fabbiano, G. 2013, *ApJ*, 776, 116
 —. 2015, *ApJ*, 812, 127
 Kravtsov, A. V., Vikhlinin, A., & Nagai, D. 2006, *ApJ*, 650, 128
 Ma, C.-P., Greene, J. E., McConnell, N., et al. 2014, *ApJ*, 795, 158
 Main, R. A., McNamara, B. R., Nulsen, P. E. J., Russell, H. R., & Vantyghe, A. N. 2017, *MNRAS*, 464, 4360
 Markevitch, M., Forman, W. R., Sarazin, C. L., & Vikhlinin, A. 1998, *ApJ*, 503, 77
 Mathews, W. G. 1990, *ApJ*, 354, 468
 Mathews, W. G., & Brighenti, F. 2003, *ApJ*, 599, 992
 Maughan, B. J., Giles, P. A., Randall, S. W., Jones, C., & Forman, W. R. 2012, *MNRAS*, 421, 1583
 McNamara, B. R., & Nulsen, P. E. J. 2007, *ARA&A*, 45, 117
 —. 2012, *New Journal of Physics*, 14, 055023
 Mei, S., Blakeslee, J. P., Côté, P., et al. 2007, *ApJ*, 655, 144
 Moore, B. 1994, *Nature*, 370, 629
 Nagai, D., Vikhlinin, A., & Kravtsov, A. V. 2007, *ApJ*, 655, 98
 Navarro, J. F., Ludlow, A., Springel, V., et al. 2010, *MNRAS*, 402, 21
 Negri, A., Posacki, S., Pellegrini, S., & Ciotti, L. 2014, *MNRAS*, 445, 1351
 Nulsen, P., Jones, C., Forman, W., et al. 2009, in *American Institute of Physics Conference Series*, Vol. 1201, American Institute of Physics
 Conference Series, ed. S. Heinz & E. Wilcots, 198–201
 Nulsen, P. E. J., McNamara, B. R., Wise, M. W., & David, L. P. 2005, *ApJ*, 628, 629
 O’Sullivan, E., Forbes, D. A., & Ponman, T. J. 2001, *MNRAS*, 328, 461
 O’Sullivan, E., Ponman, T. J., & Collins, R. S. 2003, *MNRAS*, 340, 1375
 Paturel, G., Andernach, H., Bottinelli, L., et al. 1997, *A&AS*, 124, astro-ph/9806140
 Pellegrini, S., Ciotti, L., & Ostriker, J. P. 2012, *ApJ*, 744, 21
 Pellegrini, S., & Fabbiano, G. 1994, *ApJ*, 429, 105
 Pratt, G. W., Croston, J. H., Arnaud, M., & Böhringer, H. 2009, *A&A*, 498, 361
 Puchwein, E., Sijacki, D., & Springel, V. 2008, *ApJ*, 687, L53
 Rafferty, D. A., McNamara, B. R., Nulsen, P. E. J., & Wise, M. W. 2006, *ApJ*, 652, 216
 Randall, S. W., Nulsen, P. E. J., Jones, C., et al. 2015, *ApJ*, 805, 112
 Revnivtsev, M., Churazov, E., Sazonov, S., Forman, W., & Jones, C. 2007a, *A&A*, astro-ph/0702578
 —. 2008a, *A&A*, arXiv:0804.0319
 Revnivtsev, M., Lutovinov, A., Churazov, E., et al. 2008b, *A&A*, arXiv:0805.0259
 Revnivtsev, M., Vikhlinin, A., & Sazonov, S. 2007b, *A&A*, astro-ph/0611952
 Schaye, J., Dalla Vecchia, C., Booth, C. M., et al. 2010, *MNRAS*, 402, 1536
 Shin, J., Woo, J.-H., & Mulchaey, J. S. 2016, *ApJS*, 227, 31
 Sijacki, D., & Springel, V. 2006, *MNRAS*, 371, 1025
 Sijacki, D., Springel, V., Di Matteo, T., & Hernquist, L. 2007, *MNRAS*, 380, 877
 Stanek, R., Evrard, A. E., Böhringer, H., Schuecker, P., & Nord, B. 2006, *ApJ*, 648, 956
 Su, Y., & Irwin, J. A. 2013, *ApJ*, 766, 61
 Su, Y., Irwin, J. A., White, III, R. E., & Cooper, M. C. 2015, *ApJ*, 806, 156
 Thomas, P. A., Muanwong, O., Pearce, F. R., et al. 2001, *MNRAS*, 324, 450
 Vavilova, I. B., Bolotin, Y. L., Boyarsky, A. M., et al. 2015, *Dark matter: Observational manifestation and experimental searches*
 Vikhlinin, A., Kravtsov, A., Forman, W., et al. 2006, *ApJ*, 640, 691
 Vikhlinin, A., Burenin, R. A., Ebeling, H., et al. 2009, *ApJ*, 692, 1033
 Voit, G. M. 2005, *Reviews of Modern Physics*, 77, 207
 Voit, G. M., Bryan, G. L., Balogh, M. L., & Bower, R. G. 2002, *ApJ*, 576, 601
 Werner, N., Allen, S. W., & Simionescu, A. 2012, *MNRAS*, 425, 2731
 White, III, R. E., & Sarazin, C. L. 1991, *ApJ*, 367, 476
 Willingale, R., Starling, R. L. C., Beardmore, A. P., Tanvir, N. R., & O’Brien, P. T. 2013, *MNRAS*, 431, 394
 Wong, K.-W., Irwin, J. A., Shcherbakov, R. V., et al. 2014, *ApJ*, 780, 9
 Wu, X.-P., Xue, Y.-J., & Fang, L.-Z. 1999, *ApJ*, 524, 22